BROADER PERSPECTIVES

The current status and future prospects of kesterite solar cells: a brief review

Xiaolei Liu[1]*, Yu Feng[1], Hongtao Cui[1]*, Fangyang Liu[1], Xiaojing Hao[1], Gavin Conibeer[1], David B. Mitzi[2]* and Martin Green[1]*

[1] School of Photovoltaic and Renewable Energy Engineering, University of New South Wales, Sydney, NSW 2052, Australia
[2] Department of Mechanical Engineering and Materials Science, Duke University, Durham, NC 27708-0300, USA

ABSTRACT

Kesterite-based solar cells are attracting considerable attention in recent years, owing to the reduced toxicity and greater abundance of their constituent elements. In this brief review, we discuss the current status of this important technology by focusing on three key aspects of the device: (i) the interface between the kesterite absorber and the Mo back contact, (ii) the kesterite absorber bulk defects and grain boundaries and (iii) the interface between the kesterite absorber and the buffer layer. By identifying key issues to be addressed, we provide suggestions for their potential improvement and future research. Copyright © 2016 John Wiley & Sons, Ltd.

*Correspondence

Xiaolei Liu, Hongtao Cui, and Martin Green, School of Photovoltaic and Renewable Energy Engineering, University of New South Wales, Sydney, NSW 2052, Australia and David B. Mitzi, Department of Mechanical Engineering and Materials Science, Duke University, Durham, NC 27708-0300, USA.
E-mail: frank_lin_liu@hotmail.com; h.cui@unsw.edu.au; m.green@unsw.edu.au; david.mitzi@duke.edu

1. INTRODUCTION

Thin film chalcopyrite photovoltaics based on Cu(In,Ga)Se$_2$ (CIGS) and related alloys have already demonstrated record cell efficiency of 21.7% on the laboratory scale [1]. However, the production of CIGS solar cells is expected to be limited as a result of indium scarcity and growth in its price because of high demand from the display industry. Kesterite photovoltaics utilizing Cu$_2$ZnSnS$_4$ (CZTS), Cu$_2$ZnSnSe$_4$ (CZTSe) and Cu$_2$ZnSn(S,Se)$_4$ (CZTSSe) are emerging as the most promising replacement for the chalcopyrite absorbers, through the substitution of the rarer metal indium in the CIGS absorber with comparatively abundant and lower cost zinc and tin [2–4]. These kesterite absorbers demonstrate a high absorption coefficient of 10^4 cm^{-1} and a direct band gap in the range of 1.0 to 1.5 eV, which allows for effective absorption of the incident photons in absorbers with thicknesses of a few microns [5]. With less toxic and more abundant elements (aside from the possibility of selenium), optimum band gaps and high absorption coefficients, kesterite compounds are promising

candidates for application in solar cells, although a suitable photovoltaic material requires more than optimum band gaps and high absorption coefficients, such as favorable transport properties, suitable doping level, high carrier lifetime and suitable band edge position.

The first vacuum-deposited CZTS solar cell was reported by Katagiri *et al.* with a power conversion efficiency of 0.66% in 1997 [6]. The current record CZTSSe cell efficiency of 12.6% was reported in 2013 [7]. Surprisingly, most record devices since 2009 have been achieved using a solution-based film deposition approach, contradicting the usual bias that solution-deposited films are generally lower performing compared to vacuum-deposited analogs [1,7–10]. Although noteworthy increases in conversion efficiency have been achieved in recent years, significant improvements are required in order to further enhance efficiency to the level of CIGS solar cells, and increase the commercial viability of these types of photovoltaics [1,7].

For a CZTSSe solar cell with a band gap of 1.13 eV, the Shockley–Queisser (SQ) limits for open circuit voltage (V_{oc}), short-circuit current density (J_{sc}), fill factor (FF)

and efficiency are 820 mV, 43.4 mA/cm^2, 0.871 and 31%, respectively [7,11]. However, the 12.6% efficient hydrazine-processed CZTSSe record cell only achieved a V_{oc} of 513.4 mV, a J_{sc} of 35.2 mA/cm^2 and a FF of 0.698, corresponding to 62.6%, 81.1% and 80.1% of the SQ limit values, respectively. Through the optimization of optical designs, a 12% efficient CZTSSe solar cell achieved 83% of the SQ limit of J_{sc} [11]. Despite the improvement in short circuit current, the V_{oc} deficit is the key hurdle to achieving higher efficiency in the CZTSSe devices, followed by the deficits in FF and J_{sc}.

There are several review papers on kesterite solar cells [2–5,12–26]. The aforementioned publications provide comprehensive overviews on a variety of aspects of these devices including: the properties of kesterite absorbers, such as crystal structure, phase diagram, secondary phases, chemical composition, defect physics, electronic band structure, grain boundaries (GBs), optical properties, fabrication strategies and characterization methods, and two critical interfaces, i.e. the interfaces between the kesterite absorber and the molybdenum (Mo) back contact and between the kesterite absorber and the CdS buffer layer. Although high quality review papers have been published to summarize the challenges and promise of kesterite devices, the present work aims to provide a brief update, including more recent selected studies, and to synthesize the observations to identify new pathways to highly efficient kesterite solar cells in future research.

## 2. THE INTERFACE BETWEEN THE KESTERITE ABSORBER AND THE MO BACK CONTACT

Mo films have been widely adopted as back contacts for CIGS solar cells, because they fulfill most requirements of a good back contact. These criteria include stability at high processing temperatures and resistance to alloying with Cu [27–35], excellent adhesion between the soda lime glass (SLG) substrates and CIGS absorbers, and low-resistance contact to the CIGS absorber. An intermediate layer of MoSe$_2$, formed between Mo and CIGS during the growth of CIGS, is beneficial to the ohmicity of the Mo back contact [31,32,35–37]. The beneficial effect of MoSe$_2$ was exemplified in the structure of Mo/ZrN/MoSe$_2$/CIGS [38]. The ZrN reflector layer increases the Mo back contact reflectance and improves the long wavelength quantum efficiency. However, the optical gain is offset by increased back contact recombination and contact resistance. A thin MoSe$_2$ layer was used to decrease the back contact recombination and contact resistance, therefore improving V_{oc} and FF. The MoSe$_2$ layer was formed by annealing an approximately 2-nm-thick layer of sputtered Mo for 20 min at 500 °C in a low pressure Se atmosphere [38].

Presently, the structure of CZTS devices replicates that of CIGS cells as a shortcut for development, without considering the difference between CZTS and CIGS material

systems [39]. Different from the case of CIGS, the Mo thin film back contact has been demonstrated to have some detrimental effects on CZTS device performance [26]. Cu$_2$ZnSnS(e)$_4$ is not stable at high processing temperature (500–600 °C) in the presence of Mo [40]. The reaction (1) describes the decomposition of Cu$_2$ZnSnS(e)$_4$ [40,41].

$$2Cu_2ZnSnS(e)_4 \leftrightarrow 2Cu_2S(e) + 2ZnS(e) + 2SnS(e) + 2S(e)(g) \quad (1)$$
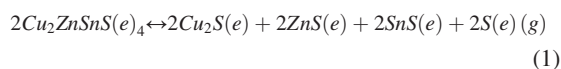
At the CZTS(e)/Mo interface, Mo reacts with S(e) to generate MoS(e)$_2$ according to the following reaction (2) [41]:

$$Mo + 2S(e) \rightarrow MoS(e)_2 \quad (2)$$
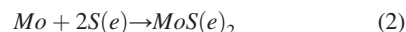
The two-stage reactions of (1) and (2) can be combined to form an equivalent reaction (3), which Scragg *et al.* proposed to describe the instability of the Mo back contact at the CZTS(e)/Mo interface during thermal processing [42]:

$$2Cu_2ZnSnS(e)_4 + Mo \rightarrow 2Cu_2S(e) + 2ZnS(e) + 2SnS(e) + MoS(e)_2. \quad (3)$$
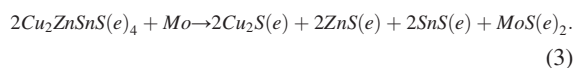
The free energy change of reaction (3) was calculated to be −100 kJ for CZTSe and −150 kJ for CZTS at 550 °C. Such negative free energy changes indicate that the decomposition reaction is thermodynamically favorable and that the CZTS(e)/Mo interface may become unstable [41,42]. The instability of the Mo back contact can potentially cause losses of V_{oc}, J_{sc} and FF in the CZTS device if not mitigated by film preparation conditions or device structure [40]. From a kinetic perspective, the formation reaction of MoS$_2$ has a fast rate. Despite a fast rate of heating and cooling being applied during sulfurization, 20-nm and 60-nm-thick MoS$_2$ can still be formed after 3 min and 10 min of annealing, respectively [26,43]. A ~1300-nm-thick MoSe$_2$ layer was observed to increase the device resistance and degrade V_{oc} [3,44].

After S(e) loss in Reaction (1), evaporation of SnS(e) is expected because of the high vapor pressures [41]. Therefore, overpressures of S(e) and SnS(e) are desirable during high temperature annealing to suppress the decomposition of CZTS(e), according to the Reaction (1) mechanism [45]. However, this high S(e) pressure results in thick MoS(e)$_2$ layers according to Reaction (2); 100- to 200-nm-thick MoS(e)$_2$ layers are observed in the best-performing CZTS(e) devices [7,42]. As Mo deteriorates the stability of CZTS(e) as shown in Reaction (3), two approaches were proposed to eliminate the detrimental effect [42]: (i) replace Mo with a more inert back contact material; (ii) use an intermediate layer between CZTS(e) and Mo to prevent the reaction of CZTS(e) and Mo. While the intermediate layer might block the out-diffusion of Na from the SLG substrate, an externally provided Na source, such as NaF [10] and Na$_2$S [46], can be intentionally introduced in

these cases to compensate for the expected low out-diffusion of Na.

A variety of metals have been investigated as back contact options for CIGS solar cells, including W, Mo, Cr, Ta, Nb, V, Ti, Mn, Au, Ni, Ag and Pt [33,37,47]. Among the metals, Ti, V, Cr and Mn films react with Se during co-evaporation of CIGS absorbers and the reaction advances during the whole CIGS deposition. Consequently, Ti and Mn may be completely consumed by the chemical reaction [37]. Pt, Ag, Au, Ti and Ni show a significant diffusion into the CIGS absorber [33,37,47,48]. Orgassa *et al.* reported that the best CIGS device efficiencies were 14.2% on W, 13.8% on Mo, 13.3% on Ta, 10% on Nb, 5.9% on Cr and 3.4% on V [37]. The CIGS devices on the back contact materials of W, Mo and Ta achieve comparable efficiencies. Hence, although Mo is commonly used in high efficiency CIGS solar cells [47], W and Ta also look somewhat promising.

Alternative back contact materials of Au, W, Pd, Pt and Ni have also been applied in the CZTS-based solar cells [26,49]. Pd and Ni were observed to diffuse into the CZTSSe absorber extensively after annealing at 570 °C for 30 min, while Au did not react with the chalcogens, W reacted partially and Pt reacted completely. Therefore, Pd, Ni and Pt are not suitable as back contact materials under the conditions examined. W and Au are eligible contact materials because of their ability to enhance short circuit current (J_{sc}). In contrast to Mo, Au is a highly reflective back contact and increases the absorption of photons in the long wavelength range, therefore enhancing J_{sc} [50]. W may serve to passivate the CZTSSe absorber and improve the collection of carriers generated deep in the absorber [49]. However, Mo remains the best choice material for a back contact, so far (i.e. it is used for all record-performing devices), and achieved the highest conversion efficiency of 4.8% in this particular study. In contrast, cells with W and Au back contacts demonstrated deteriorated efficiencies of around 3.9%. The reduced efficiency was mainly attributed to decreases in fill factor (FF) [49]. In the case of a W back contact, a ~350-nm-thick W $(S,Se)_2$ layer was generated, which increased the series resistance and reduced FF. For the Au back contact, a high density of voids was observed in the CZTSSe absorber, resulting in a very low shunt resistance and deteriorated FF. Of course, with all of the above results, it is important to keep in mind that the suitability of a back contact material will significantly depend not only on the choice of metal, but also on the specific processing approach used to deposit the CIGS or CZTSSe layer on top. For some of the above-mentioned back contact choices, it is possible that with optimization of the processing for the specific back contact material (which may not be the same best conditions as for deposition on Mo), high performance may be achieved.

Various intermediate layers have been developed to inhibit the decomposition of CZTS(e) at the Mo back contact. A TiN barrier layer deposited at the Mo/CZTS interface allows for a good grain structure at a high annealing temperature of 570 °C, while keeping $MoSe_2$ thickness within acceptable limits (<300 nm) [44]. Furthermore, the Na diffusion from the SLG is not significantly affected [40]. Consequently, a TiN barrier layer reduces the $MoSe_2$ thickness from ~1300 nm to ~220 nm and the series resistance from 3.4 Ωcm^2 to 1.8 Ωcm^2. The efficiency, V_{oc}, J_{sc} and FF increase significantly in this study. Barrier layer approaches such as this one using TiN may also open pathways to the use of other metals for the back contact, which might be overly reactive for use without the barrier layer, but which may offer advantages in terms of resistivity, work function, diffusion characteristics and mechanical hardness, if enabled by the barrier.

Lopez-Marino *et al.* applied a ZnO barrier layer to inhibit the decomposition of sputtered CZTSe in the vicinity of the Mo back contact [51]. They found that this ZnO layer improved the interface morphology and reduced the density of voids, leading to decreased series resistance from 3.7 Ωcm^2 to <0.1 Ωcm^2. Consequently, the efficiency, FF and J_{sc} improved significantly and V_{oc} increased moderately. Li and Liu *et al.* also observed that a 10-nm ZnO barrier layer reduced the MoS_2 thickness and improved the sputtered CZTS device efficiency [52,53]. Liu *et al.* found that a TiB_2 barrier layer inhibited the formation of the MoS_2 layer (like TiN), resulting in reduced series resistance and enhanced J_{sc}, FF and efficiency [54]. On the other hand, introducing a TiB_2 barrier layer between sol–gel processed CZTS and Mo degrades the CZTS crystallinity, which results in some degradation of V_{oc}. Cui *et al.* and Li *et al.* investigated the role of an Ag intermediate layer in sputtered CZTS solar cells [39,55]. The Ag intermediate layer was observed to inhibit the formation of voids at the CZTS/Mo interface, which accounts for the decreased series resistance and improved J_{sc} and FF [39]. Ag is incorporated into the CZTS crystal structure uniformly because of the high diffusivity of Ag [39,55].

Another promising intermediate layer recently developed for the CZTS/Mo interface is an ultra-thin carbon layer. CZTSSe films synthesized from binary and ternary chalcogenide nanoparticles of Cu_2SnS_3, ZnS, SnS and Cu_xS_y typically exhibit a bilayer structure, with the bottom layer comprising fine grains and the top layer consisting of densely packed large grains [56]. The bottom layer demonstrates high carbon content, in addition to CZTSSe nanoparticles and binary/ternary chalcogenide precursor nanoparticles (Figure 1). It was speculated that the high content of carbon improves the conductivity of the small-grain layer [56], even while the small-grained nature of this layer likely introduces substantial recombination. Because of the instability of Mo at the interface with the kesterite absorber, voids are often observed in the Mo back contact region. An ultra-thin and intentionally introduced carbon layer has recently been developed to act as an intermediate layer between the kesterite absorber and the Mo back contact [57], in order to reduce the void-induced series resistance that is likely to arise in this region of the device. The evaporated carbon intermediate layer increases J_{sc}
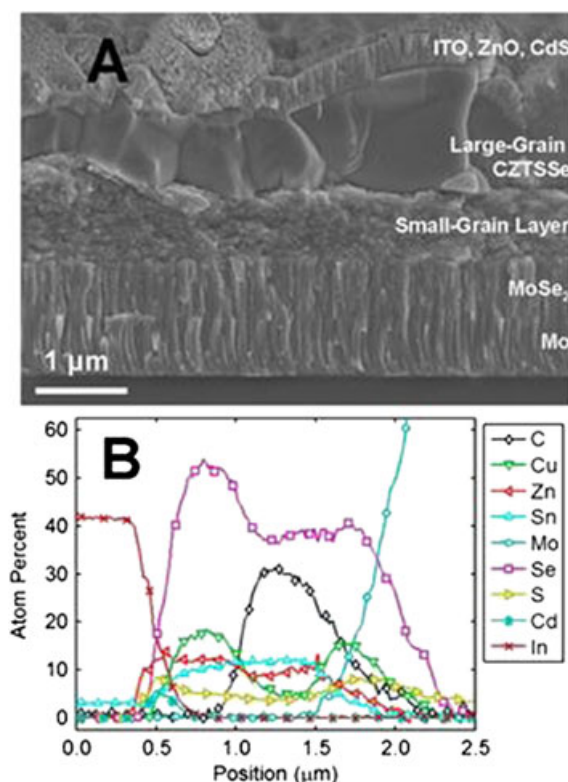
Figure 1. (a) Cross-sectional SEM image and (b) Auger depth profile of a finished CZTSSe solar cell, prepared from binary (ZnS and SnS) and ternary (copper tin sulfide) chalcogenide nanoparticles. Reprinted with permission from [56], Copyright (2012) American Chemical Society.

and conversion efficiency of CZTS devices with the absorbers fabricated by two-stage preparation, i.e. non-vacuum (sol–gel) or vacuum (sputtering) methods followed by high temperature sulfurization. Meanwhile, the carbon intermediate layer does not deteriorate V_{oc} and FF. Figure 2 shows the transmission electron microscopy (TEM) image and corresponding energy dispersive spectroscopy (EDS) mappings of the CZTS device with a carbon intermediate layer fabricated by the sol–gel method. It was observed that carbon adheres on the inner walls of voids. By comparing EDS line scans on the CZTS devices with and without the carbon intermediate layer, it was confirmed that the carbon sticking on the inner walls of voids arose from the intentionally introduced carbon layer rather than the precursor solution used in the sol–gel based method. The carbon aggregation better connects void-containing CZTS and the Mo back contact, which reduces the series resistance R_s and leads to increased J_{sc} and improved conversion efficiency [57]. The performance of kesterite devices with different intermediate layers is summarized in Table I.

3. KESTERITE ABSORBER BULK DEFECTS AND GBS

3.1. Bulk defects

Several comprehensive reviews of CZTSSe kesterite absorber bulk defects have been previously presented

[3,58,59]. In this section, we highlight the importance of antisite defects and band tailing in this complex quarternary semiconductor, and extend the discussion to include the recent indication that a low temperature post-annealing may provide one pathway to reducing the concentration of the $[Cu_{Zn} + Zn_{Cu}]$ defect complex.

First-principles calculations have indicated that the isolated anti-site defect Cu_{Zn} has the lowest formation energy and contributes to the p-type conductivity in the stoichiometric kesterite (CZTS and CZTSe) material system [58,60]. The anti-site defect Cu_{Zn} induces a relatively deep acceptor level in the band gap, which can cause Fermi-level pinning with a large concentration that in turn deteriorates the device performance. Most of the reported high efficiency kesterite solar cells exhibit copper-poor and zinc-rich conditions (i.e. $Cu/(Zn + Sn) \approx 0.85$ and $Zn/Sn = 1.1–1.3$ [61]), in which the formation energy of Cu vacancy (V_{Cu}) defects decreases accordingly. The V_{Cu} defect is a shallow acceptor and less likely to promote detrimental Fermi-level pinning. It is also possible that the anti-site defect Cu_{Zn} is formed, although the density should be relatively small. The copper-poor and zinc-rich conditions also suppress the Sn_{Zn} defect, which is a deep-level donor defect acting as a recombination center. Nevertheless, more experimental investigations are needed to validate these theoretical predictions and precisely identify the chemical origins of the full range of defects in current-generation CZTSSe.
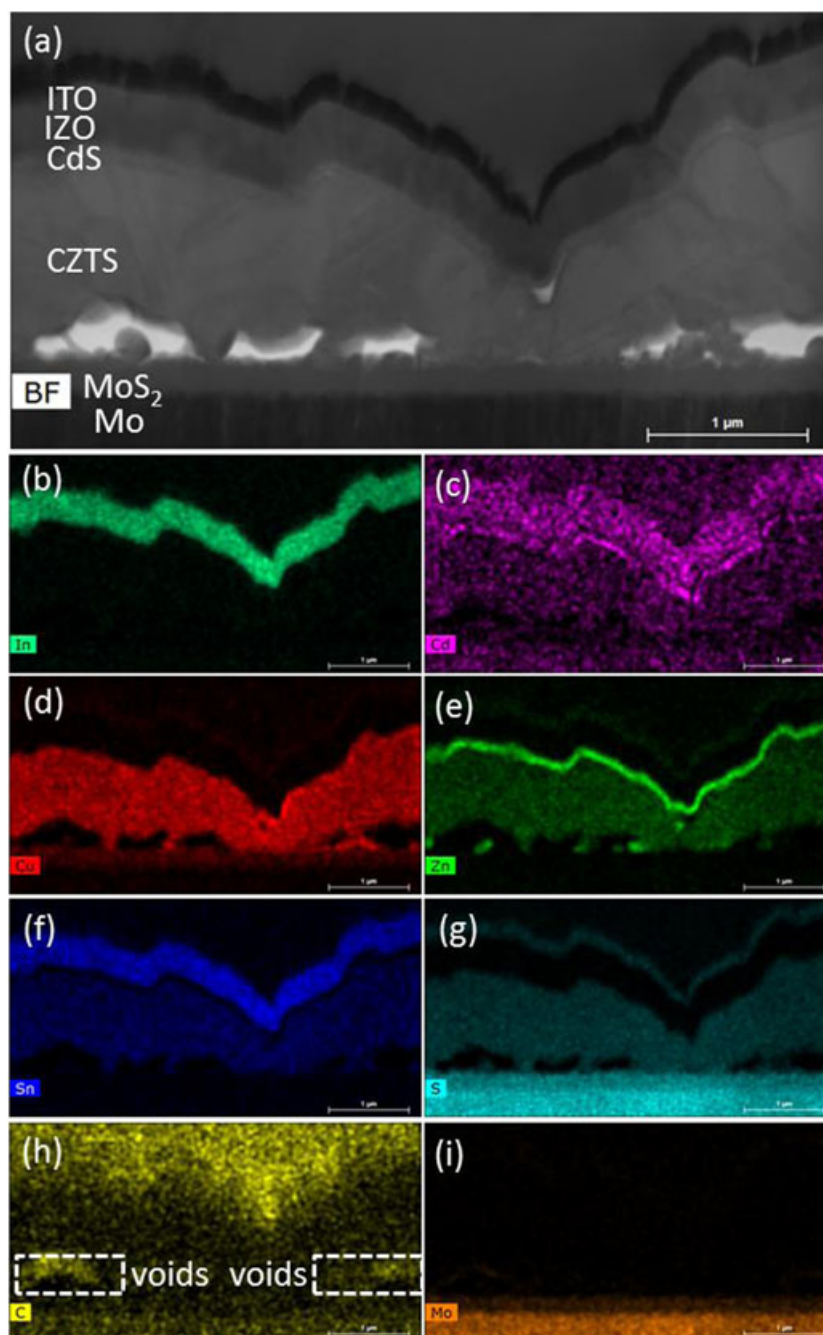
Figure 2. (a) Cross-sectional TEM image of the CZTS device with a carbon intermediate layer fabricated by the sol–gel based method and (b–i) the EDS mappings for the compositional distribution ((b) In, (c) Cd, (d) Cu, (e) Zn, (f) Sn, (g) S, (h) C and (i) Mo) in the whole area of (a). Reprinted with permission from [57], Copyright (2015) American Chemical Society.

In addition to the composition, the growth parameters (temperature and pressure) also affect the chemical potential, and consequently determine the formation energy of defects. The disequilibrium of real-world processing conditions also influence the formation of defects [3]. Fernandes *et al.* fabricated a CZTS absorber by sulfurization of a dc-sputtered stacked metallic precursor of Zn/Sn/Cu [62]. Admittance spectroscopy was applied to obtain two defect activation energies of 45 meV and 113 meV, which were attributed to the calculated defect levels of V_{Cu} and Cu_{Zn}, respectively [58,63]. Barkhouse *et al.* deposited a CZTSSe absorber by a hydrazine-based solution process [8]. Capacitance spectroscopy revealed a dominant defect level at 156 meV, which was again associated with the predicted Cu_{Zn} defect [9,58]. Therefore, the defect positions and densities appear to be somewhat changeable by modifying film

Table I. Summary of the performance of kesterite solar cells with different intermediate layers.

Reference paper	[44]	[44]	[51]	[51]	[52]	[52]	[53]	[53]	[54]	[54]	[39]	[39]	[57]	[57]
Intermediate layer	TiN	Without TiN	ZnO	Without ZnO	ZnO	Without ZnO	ZnO	Without ZnO	TiB_2	Without TiB_2	Ag	Without Ag	C	Without C
Intermediate layer thickness (nm)	20	0	10	0	10	0	10	0	30	0	20	0	25	0
Kesterite absorber	CZTSe	CZTSe	CZTSe	CZTSe	CZTS	CZTS	CZTS	CZTS	CZTS	CZTS	CZTS	CZTS	CZTS	CZTS
Annealing temperature (°C)	570	570	525	525	560	560	570	570	580	580	570	570	580	580
Annealing time (min)	5	5	45	45	60	60	30	30	60	60	30	30	40	40
Efficiency (%)	8.9	2.95	6	2.5	3.26	2.07	4.3	1.13	4.4	3.06	4.42	2.31	5.52	4.47
V_{oc} (mV)	385	264	364	314	657	475.9	641	324	598	658	598	476.9	560	560
J_{sc} (mA/cm^2)	42.6	25.4	28.6	19.7	10.75	14.52	15.97	10.8	13.21	9.56	15.05	11.92	16.96	13.6
FF (%)	54.2	44	57.5	40.2	46.1	27.9	42	32	56	49	49.2	40.7	56	55
R_s (Ω cm^2)	1.8	3.4	<0.1	3.7	27.9	26.8	15.1	19.7	10.3	22	12.8	19.5	2	5.1
R_{sh} (Ω cm^2)	NA	NA	149	44	230.4	42.1	1630	152	NA	NA	NA	NA	NA	NA
MoS(e)$_2$ thickness (nm)	MoSe$_2$: ~220	MoSe$_2$: ~1300	MoSe$_2$: hundreds of nanometers	MoSe$_2$: hundreds of nanometers	MoS$_2$: 80	MoS$_2$: ~300	MoS$_2$: 270	MoS$_2$: 384	MoS$_2$: <50	MoS$_2$: 400	MoS$_2$: 350	MoS$_2$: 350	MoS$_2$: ~200	MoS$_2$: ~200

composition and growth parameters. More experimental investigations are needed to definitively link the desired defects to composition and processing conditions, in order to improve the quality of kesterite films.

It is challenging to control the chemical composition of kesterite materials within the copper-poor and zinc-rich chemical potential window while avoiding the formation of secondary phases, because of a narrow phase stability region within the Cu_2S–SnS_2–ZnS phase diagram [64,65]. From a thermodynamic perspective, the chemical potential boundaries delineate the region within the multi-element phase diagram over which single phase CZTS and CZTSe can be prepared under equilibrium conditions [58]. Compared to the stability region of $CuInSe_2$, with the chemical potential window of In (μ_{In}) about 1.0 eV wide, the CZTSe quaternary compound shows a much narrower chemical potential range of Zn (μ_{Zn}) (less than 0.2 eV wide) and Sn (μ_{Sn}) (about 0.6 eV wide), which shows that more strict chemical potential control of Zn and Sn is required in the synthesis process. Figure 3 shows the calculated chemical potential region of μ_{Zn} and μ_{Sn} for CZTS and CZTSe, with the chemical potential of Cu (μ_{Cu}) equal to −0.2 eV. The strictest limit comes from the chemical potential of Zn, with an extremely narrow range (less than 0.2 eV wide). ZnS (ZnSe) and Cu_2SnS_3 (Cu_2SnSe_3) will form spontaneously when the amount of Zn is too great or too small, respectively. Hundreds of angstroms of single-phase ZnSe on the CZTSe surface block the photocurrent and deteriorate the CZTSe device performance [66]. However, the ZnSe layer interdiffused with several percent Cu and Sn on the CZTSe surface may not form the blocking barrier because the interdiffusion of Sn into ZnSe will lower the conduction band edge of ZnSe and reduce the effective resistance [66]. $Cu_2SnS(e)_3$ decreases V_{oc} because of its smaller band gap energy than that of the CZTS(e) absorber. Atom probe tomograph (APT) measurement revealed a complex network of CZTSe and ZnSe domains at the nanometer scale under copper-poor and zinc-rich conditions [67], which was believed to cause nanoscale compositional fluctuations.

In the stable chemical potential range of single phase kesterite absorbers, theoretical calculations have demonstrated that the CZTS and CZTSe compounds are the most stable in the kesterite crystal structure (i.e. with this specific metal cation ordering) [5,20]. However, first-principles investigation showed that the total energy difference between the kesterite (KS) and stannite (ST) structures is small, which implies that KS and ST ordering may coexist [68]. Schorr *et al.* applied neutron diffraction techniques to study the crystal structure of CZTS [69]. A partially disordered KS (PD-KS) structure was observed in their investigation, in which the atoms in the Cu + Zn (001) layer are disordered [68,69]. The disorder in the Cu + Zn layer is accounted for by the low randomization energy of 9.1 meV/atom and small volume expansion of 0.3%, which indicates a strong tendency to induce anti-site defects of Cu$_{Zn}$ and Zn$_{Cu}$. The donor–acceptor compensation pair can decrease the total formation energy relative to the sum of isolated defects
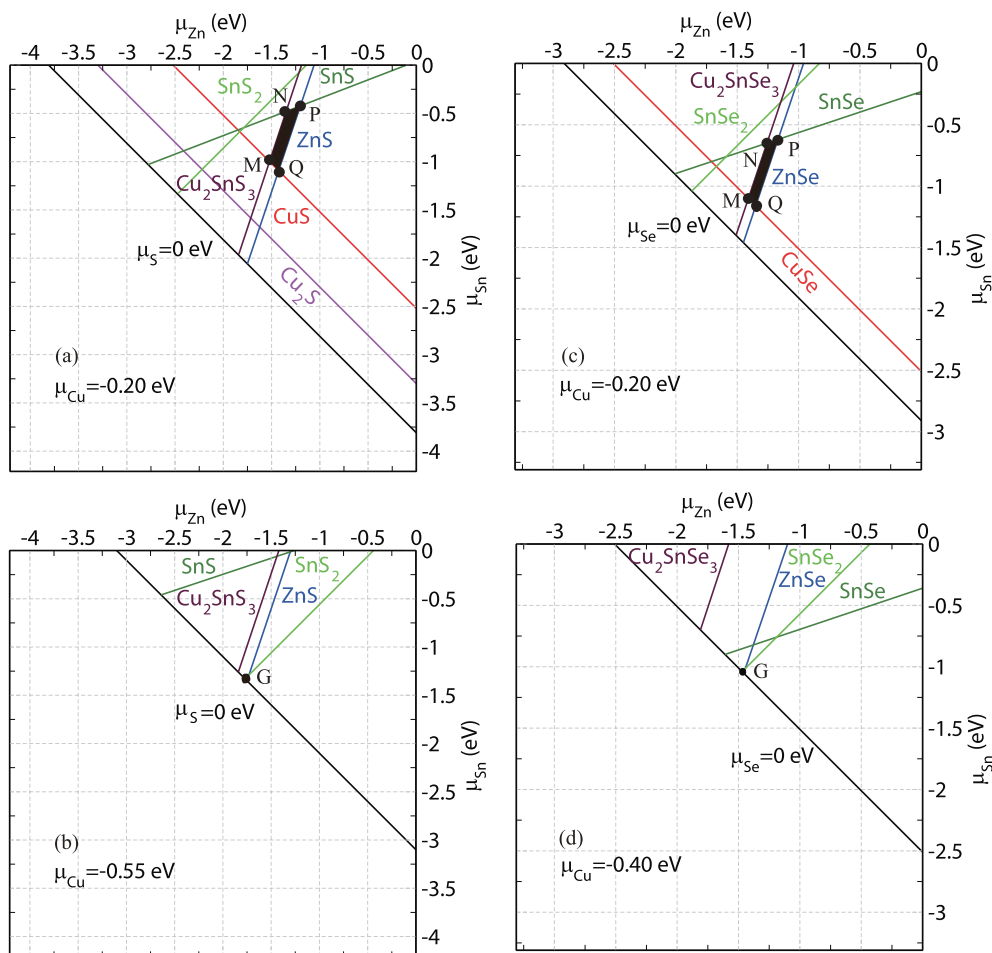
Figure 3. Stable chemical potential regions for CZTS (left) and CZTSe (right) in μ_{Zn} and μ_{Sn} with different μ_{Cu}. Reprinted with permission from [58].

[58]. Cu_{Zn} and Zn_{Cu} are the lowest formation-energy acceptor and donor defects, respectively. The donor–acceptor defect complex $[Cu_{Zn} + Zn_{Cu}]$ has an extremely low formation energy of 0.2 eV [58], which results in a high concentration of these defects. The high concentration of V_{Cu}, Cu_{Zn} and Zn_{Cu} intrinsic defects, their compensation and the local deviations in the distribution of these defects introduce potential fluctuations in the band structure [70]. These fluctuations lead to a decrease in the effective band gap energy E_g and a large V_{oc} deficit [71–76]. This band tailing is expected to be one of the principle causes of reduced V_{oc} in the CZTS and CZTSSe devices and has been noted in even the highest performing devices [73].

Photoluminescence (PL) has been applied to investigate the electronic structure in kesterite absorbers. Different models are proposed to explain the mechanism of the observed radiative transitions [77,78], such as donor–acceptor pair (DAP) recombination, free-to-bound (FB) emission and band tail induced recombination [73,77–83]. The DAP model was applied in a variety of previous studies [79,80]. However, the DAP model cannot explain the red shift of the PL peak position upon increasing temperature, which is opposite to the prediction of DAP recombination [84,85]. Therefore, the temperature dependence of the band gap was introduced in the model of DAP recombination to explain the controversial experimental results [79,80]. Recently, a model of band tailing induced by band gap fluctuations [73] and electrostatic potential fluctuations [73,77,78,82,83] was adopted in PL studies. However, the origin of PL in kesterite thin films is not clarified even today.

The model of potential fluctuations, proposed by Levanyuk and Osipov [86], is applicable to heavily doped and highly compensated semiconductors, such as CIGS chalcopyrites [84] and CZTS kesterites [87]. The fluctuating potential originates from the high concentration of charged defects [73], which are often observed in kesterite thin films [82]. At different temperatures and excitation intensities, various radiative transitions have been demonstrated, namely, band-to-impurity (BI) [78,82,83], tail-to-impurity (TI) [77], tail-to-tail (TT), band-to-tail (BT) [78,83] and band-to-band (BB) recombination [78,83]. A relatively deep acceptor level with ionization energy of ~280 meV was reported in hybrid sputtering/evaporation

processed CZTS thin films, which will influence the recombination mechanism and the efficiency of kesterite solar cells [77]. Grossberg *et al.* proposed that the observed deep acceptor defect with ionization energy of ~280 meV could be Cu_{Sn} because of slightly Cu-rich chemical composition [82]. However, Tanaka *et al.* could not clarify the origin of a deep acceptor defect according to first-principle calculation with respect to CZTS [78], which highlights the difficulty in establishing the relationship between theory and experimental measurements. Band gap fluctuations can arise from mixtures of kesterite and stannite phases, non-uniform strain, variation in chemical composition and formation of secondary phases [73]. Grossberg *et al.* measured the PL spectrum of CZTS polycrystalline powders at 10 K [82]. They attributed the PL bands at 1.35 eV and 1.27 eV to kesterite CZTS and a disordered kesterite phase respectively. Gokmen *et al.* investigated the room-temperature PL spectrum of a hydrazine-processed CZTSSe device and demonstrated that the PL band was ascribed to fluctuating potentials [73]. However, the existence of band gap fluctuations might not be ruled out in these CZTS films. Therefore, the origin of the band-edge tail states needs further investigation.

The concentration of Cu_{Zn} and Zn_{Cu} anti-site defects appears to be reduced by a low temperature post-annealing treatment [71,72]. The long-range order parameter (S) is used to describe the ordering of crystals, as calculated in Vineyard's theory of order–disorder kinetics [88]. The long-range order parameter S is in the range of 0 to 1, with 0 corresponding to complete disorder and 1 corresponding to perfect ordering. S decreases with increasing annealing temperature, and drops rapidly to zero at a critical temperature, T_c. The order–disorder transition occurs at this critical temperature, which is generally much lower than the temperature used to fabricate the kesterite films (i.e. at the formation temperature, the film will have disordered Cu/Zn). The ordering of kesterite absorbers improves after post-annealing below T_c, but deteriorates after post-annealing above T_c. The order–disorder transition was found to be reversible by repeated annealing above and below T_c, and occurs at $260 \pm 10\,°C$ [71], $200 \pm 20\,°C$ [72] and $195 \pm 5\,°C$ [89] for reactively sputtered CZTS, co-evaporated CZTSe and solution-processed CZTSSe films, respectively (Figure 4).

The Cu–Zn disorder can be probed by Raman spectroscopy because of its sensitivity to the local atomic environment [71]. Scragg *et al.* measured the 785-nm Raman spectra of nominally ordered and disordered CZTS films and calculated the ratio of $Q = I(m_{2A})/I(m_{3A})$, where $I(m_{2A})$ and $I(m_{3A})$ are the Raman peak intensities for the A modes at 288 and 304 cm^{-1}, respectively. The value of Q indicates the level of disorder, which is larger for more ordered samples and drops rapidly to a constant level when the annealing temperature exceeds T_c. Hence, Q has the same physical implication as S, which is used in Vineyard's theory of order–disorder kinetics to describe the ordering of crystals (the value of Q, however, may

extend outside the range of 0 to 1) [88]. Rey *et al.* also compared the 633-nm Raman spectra of ordered and disordered CZTSe films [72]. The ordered CZTSe film showed significantly decreased full-width at half-maximum (FWHM) for the Raman A mode at 196 cm^{-1}, which indicated that the use of appropriate annealing dramatically reduced the defect density. It was also observed that ordering significantly reduced the peak intensities of Raman modes at 221.6 cm^{-1} and 250.4 cm^{-1}, which are attributed to either the E or the B Raman active modes of the kesterite or partially disordered kesterite (PD-KS) crystal structure [90–94]. Through all of these studies, ordering annealing at a low temperature was observed to reduce the concentration of Cu_{Zn} and Zn_{Cu} defects, and consequently increased the effective E_g. Logically, if the concentration of defects is reduced, the V_{oc} deficit should improve. However, so far this has not been reported to occur in high-performance kesterite devices. Future work should continue to explore the link (or lack thereof) between ordering induced by low-temperature annealing and V_{oc} deficit in the kesterite-based devices.

As previously mentioned, the Sn_{Zn} deep-level donor defect forms a recombination center [58,95], which also increases the V_{oc} deficit. The incorporation of Ge has been recently reported to reduce the formation of the Sn_{Zn} defect to some extent [96]. The preliminary X-ray photoemission spectroscopy (XPS) results indicate that the presence of Ge inhibits the formation of the oxidation state Sn^{+2} of Sn [96], which occupies the Zn site [95]. In this study, a 10-nm-thick Ge layer was thermally evaporated on the top of a sputtered Cu/Sn/Cu/Zn metallic stack with a Ge/(Ge + Sn) ratio of 4.4%. The $Cu_2Zn(Sn_{1-x}Ge_x)Se_4$ (CZTGeSe) absorber was fabricated by annealing the whole precursor stack in a Se + Sn containing atmosphere. A small quantity of Ge was incorporated into the CZTGeSe absorber with a Ge/(Ge + Sn) ratio of 1.6%, and most Ge atoms were located at the surface and in the nearby CZTGeSe bulk. The incorporation of Ge increases the CZTGeSe grain size. It is expected that Ge_3Se_7 is formed in the selenization process (P = 1 bar and T = 550 °C), which melts at 385 °C and decomposes into a volatile $GeSe_2$ and a liquid Ge_xSe_y phase with ~85 at% of Se [97]. This liquid phase of Ge_xSe_y assists the crystal growth and increases the grain size in the upper part of the CZTGeSe absorber. It is impressive that such small quantities of Ge significantly improve V_{oc}, FF and efficiency and slightly increase J_{sc}. The performance improvement is attributed to the decreased Sn_{Zn} defect concentration to some extent and the improved crystallinity. A large amount of nanoscale inclusions of GeO_x and SnO_2 were observed around CZTGeSe GBs, and some of them were embedded in the large grains. These nanoscale inclusions might act as electron back reflectors and reduce recombination. Their impacts are still under investigation.

Nanoparticle- and hydrazine-processed Ge-doped kesterite solar cells have been previously reported [98–102]. The incorporation of Ge increases E_g, which contributes to improved V_{oc} [100–102]. Ge also boosts carrier lifetime,
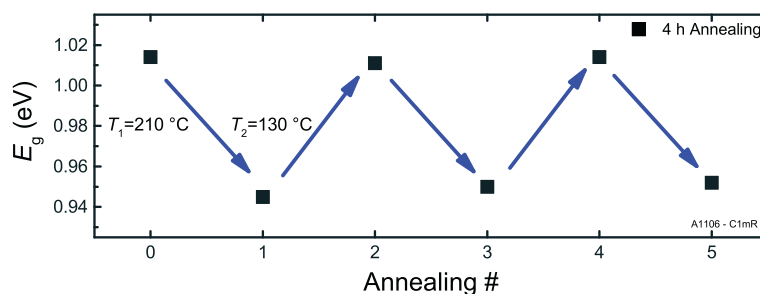
Figure 4. Band gaps measured by electroreflectance for a sample that was annealed at a temperature alternating above and below T_c for 4 h, followed by a rapid cool-down. Reprinted with permission from [89].

leading to enhanced carrier collection efficiency and J_{sc} [101]. In the nanoparticle-processed Ge-doped CZTS films, oleylamine (OLA) and trioctylphosphine oxide (TOPO) are commonly adopted as capping ligands [98]. However, these ligands are stable under an oxygen-free atmosphere, resulting in hydrocarbon impurities being left behind after high-temperature sulfurization. These impurities produce a "fine-grain" layer in a bi-layer structure (i.e. as in Figure 1). Carbon-free molecular metal chalcogenide complex (MCC) ligands, such as $Sn_2S_6^{-4}$, have been employed to eliminate the "fine-grain" layer. The MCC ligand capped CZTGeS nanocrystals (NCs) enable a carbon free, uniformly dense CZTGeS film to be formed [98]. These CZTGeS NCs were also used to fabricate CZTGeS films with a band gap grading structure (Figure 5), in which the band gap decreases monotonically toward the p–n junction [98]. Three layers of CZTGeS NCs with the band gap of ~1.84 eV, ~1.68 eV and ~1.64 eV were sequentially deposited on the Mo back contact. The band gap grading structure creates an additional quasi-electric field and helps electrons to drift toward the p–n junction. Consequently, the carrier collection efficiency and J_{sc} should increase. The band gap grading structure also produces a back surface field at the Mo back contact, which should reduce electron recombination and enhance V_{oc}.

3.2. GBs

The GBs in kesterite absorbers have been reported to exhibit nominally benign electronic properties in copper-poor and zinc-rich CZTS and CZTSSe solar cells [103]. Conductive atomic force microscopy (C-AFM) measurements show that the GBs act as electron flow channels rather than as dominant recombination centers [103]. Scanning Kelvin-probe microscopy (SKPM) measurements revealed higher positive surface potentials at the GBs in contrast to the bulk of the grains (Figure 6) [103]. The potential spike at the GBs indicates the downward band-bending in the energy band diagram. Hence, GBs act as an electrostatic potential barrier to increase charge separation in the vicinity of the GBs. This is one source of high efficiency for polycrystalline kesterite and chalcopyrite solar cells [103,104]. However, the origins of the benign potential barrier on GBs in the kesterite absorbers are still being

debated. Polizzotti *et al.* suggest that the copper-poor ordered defect compound (ODC) model may apply to CZTSSe GBs [3]. Under the Cu-poor and Zn-rich conditions, the occurrence of $[V_{Cu} + Zn_{Cu}]$ defect clusters is thermodynamically favorable. The ODC decreases both the valence and conduction band edge energies relative to the kesterite bulk. This leads to the potential barrier that attracts electrons toward GBs and repels holes from GBs. Yin *et al.* used first-principles density-functional theory (DFT) to study the properties of GBs and proposed a different theory [105]. The theoretical calculation showed that deep defects induced by the wrong bonds of Cu—Sn and Se—Se at GBs are passivated by Zn_{Sn} and O_{Se} through breaking or weakening of these bonds, which reduces GB recombination. Zn_{Sn} and O_{Se} co-passivation can also lower the valence and conduction band edge, causing the potential barrier. Although multiple theories have been proposed, more experimental studies are needed to validate these theoretical predictions.

The effect of Na on the GB has also been investigated. Sodium is beneficial for high efficiency CIGS solar cells, with SLG being the substrate of choice for most high-performance CIGS solar cells because it provides the source of sodium that can out-diffuse during the high-temperature deposition/annealing process. However, the effect of sodium on kesterite solar cells has been less thoroughly investigated. Sodium plays a role in grain growth mechanism [46]. The effect of sodium on the grain growth of kesterite absorbers has been found to exhibit a "threshold"-type behavior [106,107], where a critical concentration of sodium is essential for the growth of large grains; however, too much sodium reduces the grain size because of the formation of a secondary phase of NaCl, from the interaction of the NaF sodium source and the metal chloride precursors, and this in turn inhibits interdiffusion of constituent elements [107]. The formation of low-melting-point compounds of sodium was proposed as the mechanism to explain the enhanced grain size [106,107]. Because of the enhanced diffusivity, the liquid compounds of sodium (at the growth temperature) help remove the precipitates of ZnS under the copper-poor and zinc-rich growth conditions from an advancing GB and increase the mobility of GBs [106], thereby facilitating large grain size. However, the formation of liquid
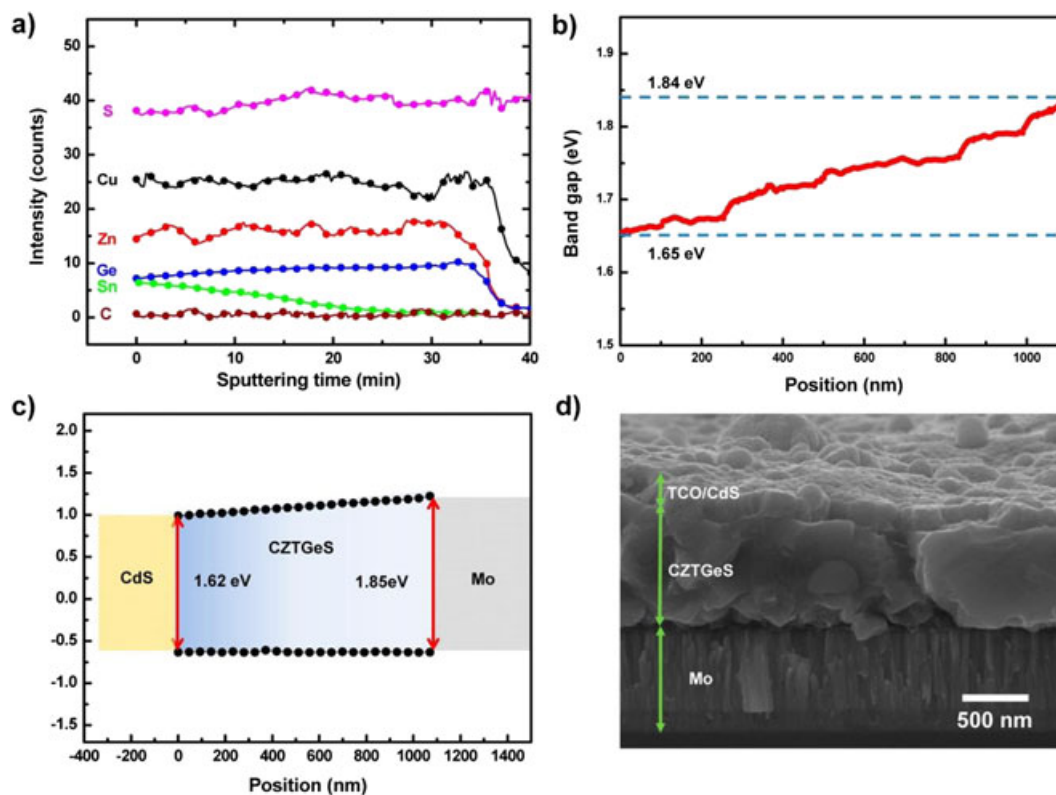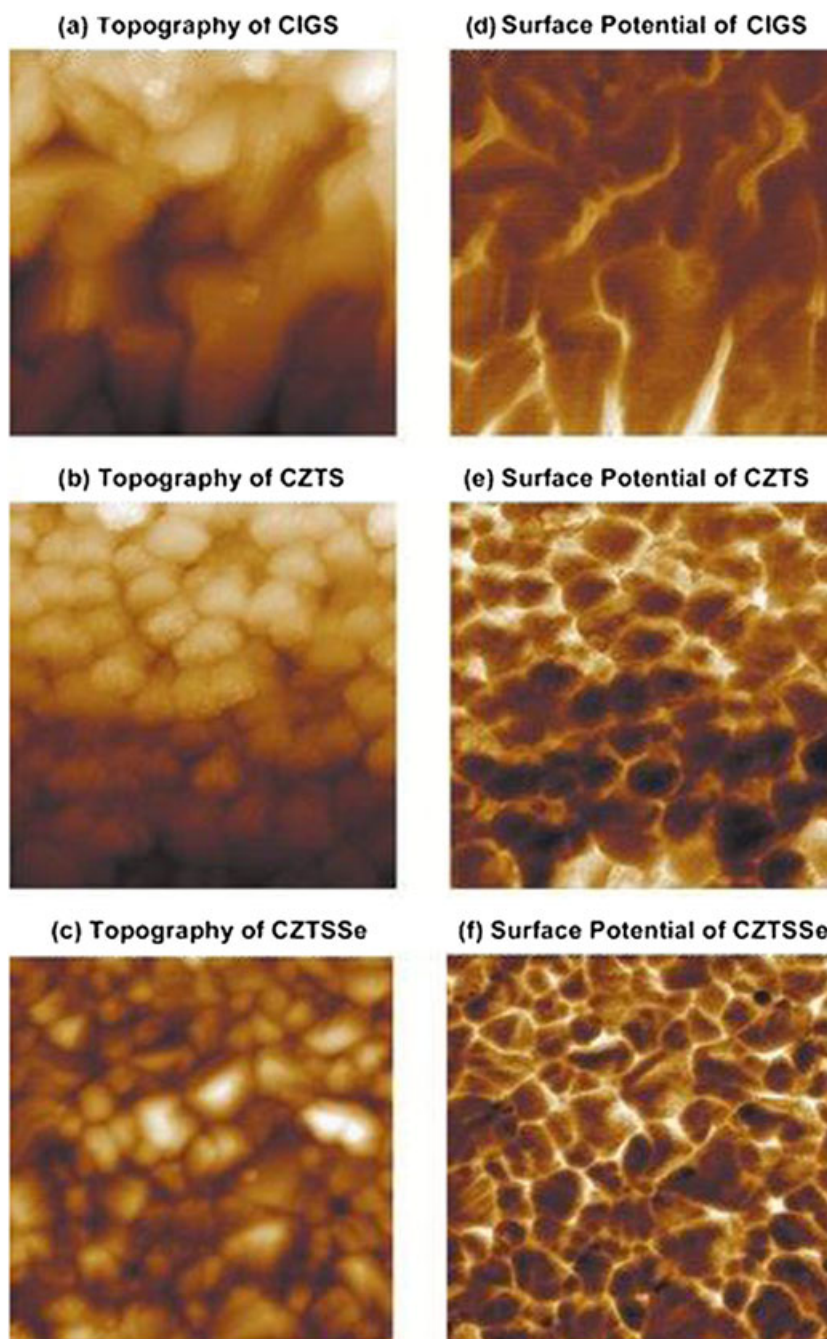
Figure 5. (a) Secondary ion mass spectrometry (SIMS) data of band gap graded annealed film to determine the compositional distribution across the Ge-containing CZTS film. (b) Sn/(Ge + Sn) ratio across the depth of the band gap graded absorber determined by SIMS measurement (a) is converted to the optical band gap using the linear relationship obtained in Figure S2 (Supporting Information [98]). (c) Band alignment of graded CZTGeS film measured by ultraviolet photoelectron spectroscopy (UPS) and inverse photoelectron spectroscopy (IPES). The band gap values were increased from 1.62 to 1.85 eV. (d) Band gap graded CZTGeS based thin film solar cell annealed under $Ar + H_2S$ (4%) at 530 °C for 30 min. Reprinted with permission from [98].

compounds of sodium has not yet been directly observed in experiments [107]. The effect of sodium on the grain size was also reported to depend on the kesterite absorber growth method and the sodium doping process [108].

Although a critical concentration of sodium is required to enhance the grain size, grain size enhancement is not necessarily the dominant factor in achieving highest device efficiency, because the effect of sodium on the electronic properties may be even more critical [106,107]. The accumulation of sodium at GBs was shown to improve the carrier collection in solution-processed CZTSSe absorbers, as revealed by electron beam induced current (EBIC) measurements [107]. Sodium was also observed to passivate the GBs and suppress the non-radiative recombination in vacuum-deposited CZTS using temperature-dependent PL spectra [106], which results in improved V_{oc}. In addition, sodium was demonstrated to increase the hole concentration in monocrystalline and polycrystalline CZTS crystals [109–111], leading to higher built-in voltage and improved V_{oc} [109,111].

Sodium plays a similar role in CIGS solar cells [112–114]. Schuler *et al.* reported that the incorporation of sodium can increase the carrier concentration of $CuGaSe_2$ crystals [114]. In their work, temperature-dependent Hall measurement was used to extract the concentration of acceptors and compensating donors and the defect activation energy. PL was applied to probe the spectroscopy of defects in the semiconductors, and combined temperature-dependent Hall measurement and PL measurement were also adopted to investigate the sodium effect on the carrier concentration [114]. From the temperature-dependent Hall measurement, it is found that sodium increases the concentration of both acceptors and compensating donors. However, the increase of the acceptor concentration is more significant than that of the compensating donor concentration, therefore resulting in the increased net carrier concentration. Because of the similarities between kesterites and chalcopyrites, the effects of sodium on these two material systems may be similar [107]. Based on this earlier work on chalcopyrites [114], four models can be formulated to explain the effect of sodium on the carrier concentration of CZTS crystals: (i) the antisite Na_{Cu} defect inhibits the

(a) Topography of CIGS

(d) Surface Potential of CIGS

(b) Topography of CZTS

(e) Surface Potential of CZTS

(c) Topography of CZTSSe

(f) Surface Potential of CZTSSe

Figure 6. Two-dimensional topography spatial maps of a) CIGS, b) CZTS and c) CZTSSe. Two-dimensional surface potential spatial maps of d) CIGS, e) CZTS and f) CZTSSe. Reprinted with permission from [103].

formation of the donor-type Zn_{Cu} defect [109], therefore reducing the compensation and increasing the carrier concentration; (ii) because of the correlation of sodium (Na) and O, Na can attract O and lead to the formation of O_s, which removes the donor-type V_s defect and increases the carrier concentration; (iii) Na forms the acceptor-type Na_{Zn} antisite defect and increases carrier concentration; and (iv) Na assists in increasing the net carrier concentration without introducing new acceptor- and compensating donor-type

defects. Further investigation is required for understanding the actual underlying mechanism of the effect of sodium on the carrier concentration.

Sodium was also reported to reduce the acceptor activation energy E_a in CZTS single crystals and to move the Fermi level toward the valence band edge, therefore allowing higher built-in voltage and V_{oc} [109]. It was observed that sodium increased the hole mobility in CZTS single crystals because of decreased defect scattering

[109], therefore reducing the resistivity of crystals and enhancing FF. Another alkali, potassium (K), was incorporated into solution-processed CZTS absorbers and the effects on the device performance were investigated [115]. The loss of Sn is often observed in the form of volatile SnS during the high temperature fabrication process. However, it is interesting to note that the incorporation of K appears to suppress Sn loss during the high temperature sulfurization process. Hence, more Zn can be incorporated during the formation of CZTS, rather than producing the secondary phase of ZnS. While, the underlying reaction mechanism demands further investigation, the CZTS Raman peak at $337\,cm^{-1}$ showed slight red shift, which suggests that K replaces the Cu site in the CZTS crystal structure. The smaller bond force constant of K—S compared to that of Cu—S results in the red shift of lattice vibrations. K doping was also demonstrated to improve crystallinity and enhance the (112) preferred orientation of CZTS thin films [115].

Because of the strong affinity between oxygen and Na ions, an air anneal of the CZTSSe film was demonstrated to facilitate the Na diffusion from the SLG substrate into the CZTSSe absorber [116]. A Mo oxide layer on the Mo back contact surface may also enhance the Na diffusion in the Mo film and lead to the formation of a Na-containing Mo oxide layer [117,118]. Oxygen also plays active roles in the kesterite absorber itself. Sardashti *et al.* investigated the effects of air annealing on the properties of hydrazine-processed CZTSSe absorbers [119]. SnO_x enrichment of GBs was observed in the air-annealed CZTSSe absorber, which formed barriers for both photo-excited holes and electrons at the GBs. These potential barriers prevent holes and electrons from entering the GBs and recombining at the GB defects. A copper-deficient CZTSSe film surface is also found to be essential for a high performance device. One mechanism used to explain this need involves Cd^{2+} ions from the CdS bath diffusing to the CZTSSe surface and forming donor states of Cd_{Cu}^{+} when the cadmium occupies the copper vacancies (V_{Cu}). A thin n-doped region then leads to the formation of a buried homojunction on the p-type CZTSSe surface, which reduces the interface recombination at the junction.

# 4. THE INTERFACE OF THE KESTERITE ABSORBER WITH THE BUFFER LAYER

The conduction band offset (CBO) of the buffer layer/kesterite absorber is one of the most critical factors in achieving high device performance [120]. A spike conformation (positive CBO) forms where the conduction band minimum of the buffer layer is higher than that of the kesterite absorber (Figure 7(a)). On the other hand, a negative value of CBO indicates a cliff conformation where the conduction band minimum of the buffer layer is lower than that of the kesterite absorber (Figure 7(b)). Theoretical analysis demonstrates that high device

performance can be achieved when the CBO at the CIGS/CdS interface is in the range of 0 to 0.4 eV [121]. When CBO is over 0.4 eV, J_{sc} decreases dramatically as the higher barrier inhibits the flow of light-generated electrons in CIGS. The cliff conformation acts as a barrier to prevent the flow of injection electrons under forward bias. The accumulation of injection electrons increases the interfacial recombination between the majority hole carriers in CIGS and accumulated electrons at the CIGS/CdS interface, thereby reducing V_{oc}. In contrast, an ideal spike conformation does not form a barrier for injection electrons and V_{oc} is nearly constant. FF decreases in the cliff conformation because of the reduced V_{oc} and from reduced current when the CBO is over 0.4 eV in the spike conformation. Consequently, CIGS/CdS devices exhibit excellent performance with a CBO of 0 eV to 0.4 eV in the spike conformation. Given the similar device configuration, the optimized CBO at the kesterite absorber/buffer layer interface is also expected to be a small spike and achieving this configuration is therefore crucial for reducing the interface recombination and achieving high kesterite device performance.

Contradictory results have been reported for the band conformation at the CZTSSe/CdS interface. Haight *et al.* [122] used femtosecond laser ultraviolet photoelectron spectroscopy on hydrazine-processed materials and noted a moderate (<0.5 eV) spike at the CZTSSe/CdS interface for all values of [S]/[S + Se] examined. Samples in this study were transferred into the measurement chamber with minimal exposure to air and a short 5 s anneal at 150–170 °C was used to remove surface adsorbed water and weakly bound contaminants. By contrast, Bär *et al.* [123] used direct and inverse photoemission on co-evaporated pure sulfide films and reported a -0.33 eV cliff-like CBO. In this case, the surfaces were cleaned by a short (10 min), mild Ar^+ treatment using an ion energy of 100 eV, rather than the gentle heating process. One of the factors causing contradictory experimental results may be the different composition of materials at the CZTSSe surface, because of different sample and surface preparation methods, which modifies the interface band structure. Various processing methods and the diffusion of ions can change the chemical composition of the surface [124].

Alternative buffer layers have been considered to not only replace the toxic CdS buffer layer but also to achieve optimal interface band alignment. Barkhouse *et al.* investigated the alternative buffer layers ZnS, ZnO and In_2S_3 [120]. Femtosecond laser pump/probe ultraviolet photoemission spectroscopy (UPS) was applied to measure the valence bands and obtain band edges of the hydrazine-processed CZTSSe absorber and buffer layers. A small negative CBO of -0.1 eV indicates the formation of cliff conformation at the CZTSSe/ZnO interface, which may reduce V_{oc} and FF because of the increased interface recombination via interface defects. Meanwhile, a large spike conformation of 1.1 eV was observed at the CZTSSe/ZnS interface, preventing photocurrent flow and hence leading to a power conversion efficiency of near zero. The CBO
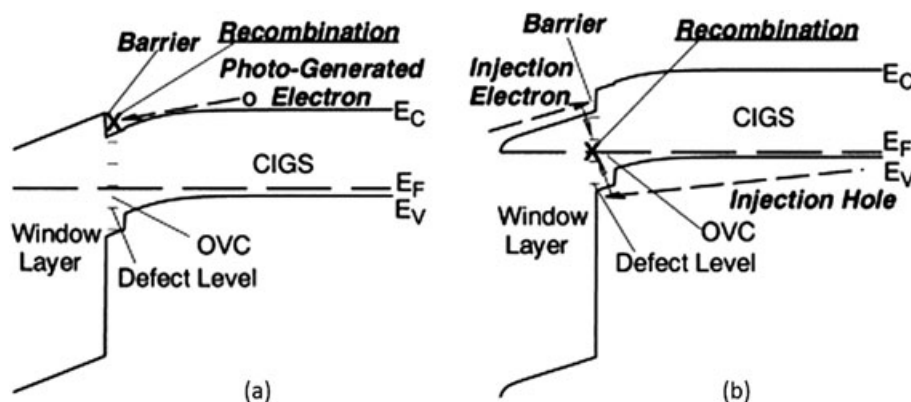
Figure 7. Schematics of energy band diagram structure in (a) spike conformation (b) cliff conformation. Reprinted with permission from [121].

at the interface of chemical bath deposition (CBD) grown ZnS and the CZTSSe absorber can be adjusted by incorporating a small amount of ZnO and Zn(OH)$_2$, as the CBO of ZnO is lower than that for ZnS [26]. A small positive spike conformation of 0.15 eV was produced between the hydrazine-processed CZTSSe absorber and an In$_2$S$_3$ buffer layer deposited by CBD, which reduces the interface recombination and does not form a barrier for the light-generated electrons. Hence a large J_{sc} and reasonable V_{oc} and FF are obtained. A CZTSSe solar cell with such an In$_2$S$_3$ buffer layer achieved an efficiency of 7.19%, which was comparable to the efficiency of 7.75% made from the analogous CdS buffer layer [120].

The use of radio-frequency (RF) magnetron sputtered (Zn,Mg)O films as an alternative to the CdS buffer layer has been reported [125]. This (Zn,Mg)O buffer layer, deposited directly on the evaporated CZTSSe absorber, damaged the CZTSSe surface and significantly reduced the efficiency. A 10-nm CdS layer was deposited between the CZTSSe absorber and (Zn,Mg)O buffer layer to suppress the sputtering damage. The efficiency of about 7% achieved with the thin CdS layer and (Zn,Mg)O buffer layer was comparable to that of the reference cell with a 60-nm-thick CdS buffer layer. The implementation of a (Zn,Mg)O buffer layer can therefore allow for a reduction of the thickness of the CdS layer while maintaining the same efficiency.

As atomic layer deposition (ALD) is a soft chemical deposition method, it can be adopted to deposit the (Zn, Mg)O buffer layer on the kesterite absorber directly. ALD-(Zn, Mg)O buffer layers have been applied in CIGS solar cells [126,127] and an efficiency of 18.1% has been achieved with the CIGS cell structure of glass/Mo/CIGS/(Zn,Mg)O buffer layer/i-ZnO/ZnO:Al [127]. The band gap energy of the (Zn,Mg)O buffer layer can be tuned by varying the amount of Mg source of bis-cyclopentadienyl magnesium [Mg(C$_5$H$_5$)$_2$] in the ALD process [127]. Given that the valance band maximum (E_v) of (Zn,Mg)O is almost constant, the conduction band minimum (E_c) can be modified by varying the Mg content. Therefore, ALD provides a

potential method to control the CBO between the kesterite absorber and the (Zn,Mg)O buffer layer.

A hybrid buffer layer of In$_2$S$_3$/CdS has also been applied, with the core aim being to enhance V_{oc} and boost efficiency [128]. An ultrathin In$_2$S$_3$ layer was deposited on top of a conventional CdS buffer layer, and then briefly (seconds to minutes) annealed at 250 to 300 °C. Significant diffusion of the indium into the CdS buffer layer and hydrazine-processed CZTSSe absorber was evident. Indium could substitute for Cd in CdS (In$_{Cd}$) to provide n-type doping, and for Sn in CZTSSe (In$_{Sn}$) leading to p-type doping. This In-doping may therefore increase the carrier concentration in both the CdS and CZTS layers, which would in turn enhance the conductivity and shift the Fermi levels in each of the materials closer to the band edges. This doping effect relieved the typically observed collapse of efficiency for temperatures below 200 K and V_{oc} saturation with the increasing sun intensity, caused by the low conductivity of the pristine CZTSSe absorbers [129]. The enhanced V_{oc} in the hybrid buffer samples is likely at least partially attributable to increasing carrier concentration in the CZTSSe absorber. Hiroi *et al.* also demonstrated a 9.2% efficiency CZTS sub-module by applying an In/Cd based hybrid buffer layer [130]. Compared with the conventional CdS buffer layer, the In/Cd based hybrid buffer layer boosts V_{oc} by over 50 mV. The application of an In/Cd based hybrid buffer layer was also observed to have increased band-bending at the CZTS surface. It was suggested that indium could substitute for Cu (In$_{Cu}$) at the CZTS surface, leading to an n-type inversion layer and enlarged band-bending. However, to fully understand these effects, further investigations are needed.

Repins *et al.* demonstrated that oxidation of a Zn-rich cap layer on co-evaporated CZTSe surfaces prior to CdS deposition provided an absolute increase to FF of approximately 5% [10]. The Zn-rich cap layer was produced by applying a reduced but non-zero Zn rate during the cool-down period of the co-evaporation process for fabricating the CZTSe absorber. Post-deposition annealing was not beneficial in an N$_2$ environment, or without the Zn-rich

cap layer, or when performed on the completed device structure. In later work, the Zn-rich cap was found to result in a distinct-phase, ZnSe [131], that increased device voltage [66]. Li *et al.* observed a similar effect of the Zn binary at the interface [132]. Thus, it is likely that the oxygen anneal results in a partial replacement of the Se by O in ZnSe. This lowers the conduction band-edge and reduces the effective resistance, resulting in the observed FF increase (Ingrid Repins, personal communication). Although oxygen passivation may remove the deep-level defect V_{Se} and reduce recombination at the CZTSe surface [3,58,133], the beneficial effect of annealing only occurred when a Zn-rich cap was present in this study. A CZTSe/Zn(Se,O)/CdS structure was applied to achieve 9.15% power conversion efficiency in a device based on co-evaporated CZTSe [10].

An alternative method to adjust the interface of the kesterite absorber and the CdS buffer layer is to modify properties of the CdS buffer layer. While Tanaka *et al.* reported the post-annealing of the CdS buffer layer at 200 °C for 30 min in air [134], the cause of any device performance change was not discussed in detail. Oxygenated CdS (CdS:O) is widely used as the n-type window layer in high efficiency CdTe solar cells [135]. The CdS:O was deposited in these earlier studies by reactive sputtering in an Ar/O_2 ambient. The oxygen composition was adjusted by controlling the fraction of O_2 flow rate in the total flow rate of Ar and O_2. The optical band gap energy of CdS:O increases with increased oxygen composition, which reduces the short wavelength light absorption in the CdS window layer and increases J_{sc}. It is also possible that the increased band gap energy of CdS:O modifies the CBO at the CdTe/CdS interface and reduces the interface recombination, leading to improved V_{oc} and FF at 6% oxygen composition. The oxygenated CdS buffer layer may also be beneficial for the performance of kesterite solar cells as well by increasing the transparency of the CdS buffer layer and adjusting the CBO at the interface of the kesterite absorber and the CdS buffer layer. However, reactive sputtering is likely to damage the surface of kesterite absorbers. As an area of future exploration, in order to suppress the sputtering damage, an ultra-thin CdS layer is proposed to be CBD deposited between the kesterite absorber and the reactively sputtered CdS:O layer. Note that, for the CBD deposited CdS buffer layer itself, oxide and hydroxide incorporation can be expected.

5. CONCLUSIONS

In this brief review, we discussed current issues relating to the kesterite absorber/Mo back contact interface, the kesterite absorber bulk defects and GBs, and the kesterite absorber/buffer layer interface. Although significant progress in kesterite solar cell performance has been achieved in recent years, substantial further improvements are necessary to reach the high efficiency (>18%) required for practical application of these cell types. Some research areas

are identified to accelerate this process. First, and perhaps most importantly, the defects in the kesterite bulk need to be reduced to suppress the band tailing and the band-edge potential fluctuation. A low temperature post-annealing treatment is observed to reduce the concentration of Cu_{Zn} and Zn_{Cu} defects and consequently increase the effective E_g. However, the expected improvement of V_{oc} deficit has not been reported in high-efficiency kesterite devices, and further work is required to understand this lack of correlation. The incorporation of Ge may provide a means to reduce the detrimental Sn_{Zn} defect concentration and improve the kesterite crystal quality, leading to a decreased V_{oc} deficit. Passivation of the defects at the GBs of the kesterite absorber and at the kesterite absorber/buffer layer interface can reduce recombination and decrease V_{oc} deficit and both sodium/potassium and oxygen treatment are found to play a significant role in this passivation process.

Second, chemical composition and fabrication methods need to be controlled within the narrow phase stability window to eliminate the secondary phases formed under the copper-poor and zinc rich conditions required for detrimental defect reduction. A high S(e) pressure during annealing is typically adopted in the fabrication of high-performance devices to suppress decomposition of the kesterite absorber at the kesterite absorber/Mo interface. The side effect of the high S (e) pressure, however, is to increase the $MoS(e)_2$ thickness. While a more inert back contact material or a barrier layer at the kesterite absorber/Mo interface may be applied to reduce the $MoS(e)_2$ thickness, the effect of this substitution on the kesterite absorber growth needs further investigations.

Finally, an ideal spike-like conformation of the CBO at the buffer layer/kesterite absorber interface is critical to reduce interface recombination. This ideal spike-like conformation can be achieved by adjusting the band structure of the buffer layer or by creating an n-type inversion layer on the surface of the p-type kesterite absorber. A number of alternative buffer layer materials have been explored, including ZnS, ZnO, (Zn, Mg)O, In_2S_3 and composite CdS/In_2S_3. While so far none of these alternatives have led to devices with efficiency that can surpass that achieved with a CdS buffer layer, the phase space of potential buffer materials is quite large and has just begun to be explored.

REFERENCES

1. Green MA, Emery K, Hishikawa Y, Warta W, Dunlop ED. Solar cell efficiency tables (version 46). *Progress in Photovoltaics: Research and Applications* 2015; **23**: 805–812.

2. Repins IL, Romero MJ, Li JV, Wei S-H, Kuciauskas D, Jiang C-S, Beall C, Dehart C, Mann J, Hsu W-C, Teeter G, Goodrich A, Noufi R. Kesterite successes, ongoing work, and challenges: a perspective from vacuum deposition. *IEEE Journal of Photovoltaics* 2012; **2**: 1–7.

3. Polizzotti A, Repins IL, Noufi R, Wei S-H, Mitzi DB. The state and future prospects of kesterite photovoltaics. *Energy & Environmental Science* 2013; **6**: 3171.

4. Zhou H, Hsu W-C, Duan H-S, Bob B, Yang W, Song T-B, Hsu C-J, Yang Y. CZTS nanocrystals: a promising approach for next generation thin film photovoltaics. *Energy & Environmental Science* 2013; **6**: 2822.

5. Mitzi DB, Gunawan O, Todorov TK, Wang K, Guha S. The path towards a high-performance solution-processed kesterite solar cell. *Solar Energy Materials and Solar Cells* 2011; **95**: 1421–1436.

6. Katagiri H, Sasaguchi N, Hando S, Hoshimo S, Ohashi J, Yokota T. Ppreparation and evaluation of CZTS thin films by sulfurization of E-B evaporated precursors. *Solar Energy Materials and Solar Cells* 1997; **49**: 407–414.

7. Wang W, Winkler MT, Gunawan O, Gokmen T, Todorov TK, Zhu Y, Mitzi DB. Device characteristics of CZTSSe thin-film solar cells with 12.6% efficiency. *Advanced Energy Materials* 2013, DOI:10.1002/aenm.201301465

8. Todorov TK, Reuter KB, Mitzi DB. High-efficiency solar cell with Earth-abundant liquid-processed absorber. *Advanced Materials* 2010; **22**: E156–9.

9. Barkhouse DAR, Gunawan O, Gokmen T, Todorov TK, Mitzi DB. Device characteristics of a 10.1% hydrazine-processed Cu2ZnSn(Se,S)4 solar cell. *Progress in Photovoltaics: Research and Applications* 2012; **20**: 6–11.

10. Repins I, Beall C, Vora N, DeHart C, Kuciauskas D, Dippo P, To B, Mann J, Hsu WC, Goodrich A, Noufi R. Co-evaporated Cu2ZnSnSe4 films and devices. *Solar Energy Materials and Solar Cells* 2012; **101**: 154–159.

11. Winkler MT, Wang W, Gunawan O, Hovel HJ, Todorov TK, Mitzi DB. Optical designs that improve the efficiency of Cu2ZnSn(S,Se)4 solar cells. *Energy & Environmental Science* 2014; **7**: 1029.

12. Katagiri H, Jimbo K, Maw WS, Oishi K, Yamazaki M, Araki H, Takeuchi A. Development of CZTS-based thin film solar cells. *Thin Solid Films* 2009; **517**: 2455–2460.

13. Wang H. Progress in thin film solar cells based on Cu2ZnSnS4. *International Journal of Photoenergy* 2011; **2011**: 10.

14. Delbos S, Kësterite thin films for photovoltaics: a review. *EPJ Photovoltaics* 2012; **3**: 35004.

15. Ramasamy K, Malik MA, O'Brien P. Routes to copper zinc tin sulfide Cu2ZnSnS4 a potential material for solar cells. *Chemical Communications (Cambridge, England)* 2012; **48**: 5703–5714.

16. Hossain MI. Prospects of CZTS solar cells from the perspective of material properties fabrication methods and current research challenges. *Chalcogenide Letters* 2012; **9**: 231–242.

17. Abermann S, Non-vacuum processed next generation thin film photovoltaics: towards marketable efficiency and production of CZTS based solar cells. *Solar Energy* 2013; **94**: 37–70.

18. Suryawanshi MP, Agawane GL, Bhosale SM, Shin SW, Patil PS, Kim JH, Moholkar AV. CZTS based thin film solar cells: a status review. *Materials Technology: Advanced Performance Materials* 2013; **28**: 98–109.

19. Azimi H, Hou Y, Brabec CJ. Towards low-cost, environmentally friendly printed chalcopyrite and kesterite solar cells. *Energy & Environmental Science* 2014; **7**: 1829.

20. Song X, Ji X, Li M, Lin W, Luo X, Zhang H. A review on development prospect of CZTS based thin film solar cells. *International Journal of Photoenergy* 2014; **2014**: 1–11.

21. Peter LM. Electrochemical routes to earth-abundant photovoltaics: a minireview. *Electrochemistry Communications* 2015; **50**: 88–92.

22. Vanalakar SA, Agawane GL, Shin SW, Suryawanshi MP, Gurav KV, Jeon KS, Patil PS, Jeong CW, Kim JY, Kim JH. A review on pulsed laser deposited CZTS thin films for solar cell applications. *Journal of Alloys and Compounds* 2015; **619**: 109–121.

23. Siebentritt S, Schorr S. Kesterites—a challenging material for solar cells. *Progress in Photovoltaics: Research and Applications* 2012; **20**: 512–519.

24. Fella CM, Romanyuk YE, Tiwari AN. Technological status of Cu2ZnSn(S,Se)4 thin film solar cells. *Solar Energy Materials and Solar Cells* 2013; **119**: 276–277.

25. Mitzi DB, Gunawan O, Todorov TK, Barkhouse DA. Prospects and performance limitations for Cu–Zn–Sn–S–Se photovoltaic technology. *Philos Trans A Math Phys Eng Sci* 2013; **371**: 20110432.

26. Huang TJ, Yin X, Qi G, Gong H. CZTS-based materials and interfaces and their effects on the performance of thin film solar cells. *physica status solidi (RRL)—Rapid Research Letters* 2014; **08**: 735–762.

27. Scofield JH, Duda A, Albin D, Ballard BL, Predecki PK. Sputtered molybdenum bilayer back contact for copper indium diselenide-based polycrystalline thin-film solar cells. *Thin Solid Films* 1995; **260**: 26–31.

28. Zoppi G, Beattie NS, Major JD, Miles RW, Forbes I. Electrical, morphological and structural properties of RF magnetron sputtered Mo thin films for application in thin film photovoltaic solar cells. *Journal of Materials Science* 2011; **46**: 4913–4921.

29. Dai X, Zhou A, Feng L, Wang Y, Xu J, Li J. Molybdenum thin films with low resistivity and superior adhesion deposited by radio-frequency magnetron sputtering at elevated temperature. *Thin Solid Films* 2014; **567**: 64–71.

30. Pethe SA, Takahashi E, Kaul A, Dhere NG. Effect of sputtering process parameters on film properties of molybdenum back contact. *Solar Energy Materials and Solar Cells* 2012; **100**: 1–5.

31. Salomé PMP, Malaquias J, Fernandes PA, Cunha AF. Mo bilayer for thin film photovoltaics revisited. *Journal of Physics D: Applied Physics* 2010; **43**: 345501.

32. Wu H-M, Liang S-C, Lin Y-L, Ni C-Y, Bor H-Y, Tsai D-C, Shieu F-S. Structure and electrical properties of Mo back contact for Cu(In, Ga)Se2 solar cells. *Vacuum* 2012; **86**: 1916–1919.

33. Wang S-F, Yang H-C, Liu C-F, Bor H-YY. Characteristics of bilayer molybdenum films deposited using RF sputtering for back contact of thin film solar cells. *Advances in Materials Science and Engineering* 2014; **2014**: 1–6.

34. Su C-Y, Liao K-H, Pan C-T, Peng P-W. The effect of deposition parameters and post treatment on the electrical properties of Mo thin films. *Thin Solid Films* 2012; **520**: 5936–5939.

35. Li Z-H, Cho E-S, Kwon SJ. Molybdenum thin film deposited by in-line DC magnetron sputtering as a back contact for Cu(In,Ga)Se2 solar cells. *Applied Surface Science* 2011; **257**: 9682–9688.

36. Jubault M, Ribeaucourt L, Chassaing E, Renou G, Lincot D, Donsanti F. Optimization of molybdenum thin films for electrodeposited CIGS solar cells. *Solar Energy Materials and Solar Cells* 2011; **95**: S26–S31.

37. Orgassa K, Schock HW, Werner JH. Alternative back contact materials for thin film Cu(In,Ga)Se2 solar cells. *Thin Solid Films* 2003; **431–432**: 387–391.

38. Malmström J, Schleussner S, Stolt L. Enhanced back reflectance and quantum efficiency in Cu(In,Ga)Se2 thin film solar cells with a ZrN back reflector. *Applied Physics Letters* 2004; **85**: 2634–2636.

39. Cui H, Liu X, Liu F, Hao X, Song N, Yan C. Boosting Cu2ZnSnS4 solar cells efficiency by a thin Ag intermediate layer between absorber and back contact. *Applied Physics Letters* 2014; **104**: 041115.

40. Scragg JJ, Kubart T, Wätjen JT, Ericson T, Linnarsson MK, Platzer-Björkman C. Effects of back contact instability on Cu2ZnSnS4 devices and processes. *Chemistry of Materials* 2013; **25**: 3162–3171.

41. Scragg JJ, Dale PJ, Colombara D, Peter LM. Thermodynamic aspects of the synthesis of thin-film materials for solar cells. *Chemphyschem* 2012; **13**: 3035–46.

42. Scragg JJ, Watjen JT, Edoff M, Ericson T, Kubart T, Platzer-Bjorkman C. A detrimental reaction at the molybdenum back contact in Cu2ZnSn(S,Se)4 thin-film solar cells. *Journal of the American Chemical Society* 2012; **134**: 19330–3.

43. Wätjen JT, Scragg JJ, Ericson T, Edoff M, Platzer-Björkman C. Secondary compound formation revealed by transmission electron microscopy at the Cu2ZnSnS4/Mo interface. *Thin Solid Films* 2013; **535**: 31–34.

44. Shin B, Zhu Y, Bojarczuk NA, Jay Chey S, Guha S. Control of an interfacial MoSe2 layer in Cu2ZnSnSe4 thin film solar cells: 8.9% power conversion efficiency with a TiN diffusion barrier. *Applied Physics Letters* 2012; **101**: 053903.

45. Redinger A, Berg DM, Dale PJ, Djemour R, Gutay L, Eisenbarth T, Valle N, Siebentritt S, Route toward high-efficiency single-phase Cu2ZnSn(S,Se)4 thin-film solar cells: model experiments and literature review. *IEEE Journal of Photovoltaics* 2011; **1**: 200–206.

46. Hlaing Oo WM, Johnson JL, Bhatia A, Lund EA, Nowell MM, Scarpulla MA. Grain size and texture of Cu2ZnSnS4 thin films synthesized by cosputtering binary sulfides and annealing: effects of processing conditions and sodium. *Journal of Electronic Materials* 2011; **40**: 2214–2221.

47. Martínez MA, Guillén C. Comparison between large area dc-magnetron sputtered and e-beam evaporated molybdenum as thin film electrical contacts. *Journal of Materials Processing Technology* 2003; **143–144**: 326–331.

48. Zhang S, *Organic Nanostructured Thin Film Devices and Coatings for Clean Energy*. CRC press: Boca Raton, FL, USA, 2010.

49. Altamura G, Grenet L, Roger C, Roux F, Reita V, Fillon R, Fournier H, Perraud S, Mariette H. Alternative back contacts in kesterite Cu2ZnSn(S1−xSex)4 thin film solar cells. *Journal of Renewable and Sustainable Energy* 2014; **6**: 011401.

50. Li-Kao ZJ, Naghavi N, Erfurth F, Guillemoles JF, Gérard I, Etcheberry A, Pelouard JL, Collin S, Voorwinden G, Lincot D. Towards ultrathin copper indium gallium diselenide solar cells: proof of

concept study by chemical etching and gold back contact engineering. *Progress in Photovoltaics: Research and Applications* 2012; **20**: 582–587.

51. Lopez-Marino S, Placidi M, Perez-Tomas A, Llobet J, Izquierdo-Roca V, Fontane X, Fairbrother A, Espindola-Rodriguez M, Sylla D, Perez-Rodriguez A, Saucedo E. Inhibiting the absorber/Mo-back contact decomposition reaction in $Cu_2ZnSnSe_4$ solar cells: the role of a ZnO intermediate nanolayer. *Journal of Materials Chemistry A* 2013; **1**: 8338–8343.

52. Li W, Chen J, Cui H, Liu F, Hao X. Inhibiting MoS_2 formation by introducing a ZnO intermediate layer for Cu_2ZnSnS_4 solar cells. *Materials Letters* 2014; **130**: 87–90.

53. Liu X, Cui H, Li W, Song N, Liu F, Conibeer G, Hao X. Improving Cu_2ZnSnS_4 (CZTS) solar cell performance by an ultrathin ZnO intermediate layer between CZTS absorber and Mo back contact. *physica status solidi (RRL) – Rapid Research Letters* 2014; **9999**. DOI:10.1002/pssr.201409052

54. Liu F, Sun K, Li W, Yan C, Cui H, Jiang L, Hao X, Green MA. Enhancing the Cu_2ZnSnS_4 solar cell efficiency by back contact modification: Inserting a thin TiB_2 intermediate layer at Cu_2ZnSnS_4/Mo interface. *Applied Physics Letters* 2014; **104**: 051105.

55. Li W, Liu X, Cui H, Huang S, Hao X. The role of Ag in $(Ag,Cu)_2ZnSnS_4$ thin film for solar cell application. *Journal of Alloys and Compounds* 2015; **625**: 277–283.

56. Cao Y, Denny MS, Jr., Caspar JV, Farneth WE, Guo Q, Ionkin AS, Johnson LK, Lu M, Malajovich I, Radu D, Rosenfeld HD, Choudhury KR, Wu W. High-efficiency solution-processed $Cu_2ZnSn(S,Se)_4$ thin-film solar cells prepared from binary and ternary nanoparticles. *Journal of the American Chemical Society* 2012; **134**: 15644–7.

57. Zhou F, Zeng F, Liu X, Liu F, Song N, Yan C, Pu A, Park J, Sun K, Hao X. Improvement of J_{sc} in a Cu_2ZnSnS_4 solar cell by using a thin carbon intermediate layer at the Cu_2ZnSnS_4/Mo interface. *ACS Applied Materials & Interfaces* 2015; **7**: 22868–22873.

58. Chen S, Walsh A, Gong XG, Wei SH. Classification of lattice defects in the kesterite Cu_2ZnSnS_4 and $Cu_2ZnSnSe_4$ earth-abundant solar cell absorbers. *Advanced Materials* 2013; **25**: 1522–39.

59. Walsh A, Chen S, Wei S-H, Gong X-G. Kesterite thin-film solar cells: advances in materials modelling of Cu_2ZnSnS_4. *Advanced Energy Materials* 2012; **2**: 400–409.

60. Chen S, Gong XG, Walsh A, Wei S-H. Defect physics of the kesterite thin-film solar cell absorber Cu_2ZnSnS_4. *Applied Physics Letters* 2010; **96**: 021902.

61. Katagiri H, Jimbo K, Development of rare metal-free CZTS-based thin film solar cells. in *37th IEEE Photovoltaic Specialists Conference* (*PVSC*). 2011.

62. Fernandes PA, Salomé PMP, da Cunha AF, Schubert B-A. Cu_2ZnSnS_4 solar cells prepared with sulphurized dc-sputtered stacked metallic precursors. *Thin Solid Films* 2011; **519**: 7382–7385.

63. Fernandes PA, Sartori AF, Salomé PMP, Malaquias J, da Cunha AF, Graça MPF, González JC. Admittance spectroscopy of Cu_2ZnSnS_4 based thin film solar cells. *Applied Physics Letters* 2012; **100**: 233504.

64. Olekseyuk ID, Dudchak IV, Piskach LV. Phase equilibria in the Cu_2S–ZnS–SnS_2 system. *Journal of Alloys and Compounds* 2004; **368**: 135–143.

65. Todorov TK, Tang J, Bag S, Gunawan O, Gokmen T, Zhu Y, Mitzi DB. Beyond 11% efficiency: characteristics of state-of-the-art $Cu_2ZnSn(S,Se)_4$ solar cells. *Advanced Energy Materials* 2013; **3**: 34–38.

66. Repins IL, Li JV, Kanevce A, Perkins CL, Steirer KX, Pankow J, Teeter G, Kuciauskas D, Beall C, Dehart C, Carapella J, Bob B. Park JS, Wei SH. Effects of deposition termination on $Cu_2ZnSnSe_4$ device characteristics. *Thin Solid Films* 2015; **582**: 184–187.

67. Schwarz T, Cojocaru-Miredin O, Choi P, Mousel M, Redinger A, Siebentritt S, Raabe D. Atom probe study of $Cu_2ZnSnSe_4$ thin-films prepared by co-evaporation and post-deposition annealing. *Applied Physics Letters* 2013; **102**: 042101–4.

68. Chen S, Gong XG, Walsh A, Wei S-H. Crystal and electronic band structure of Cu_2ZnSnX_4 (X = S and Se) photovoltaic absorbers: first-principles insights. *Applied Physics Letters* 2009; **94**: 041903.

69. Schorr S, Hoebler H-J, Tovar M. A neutron diffraction study of the stannite–kesterite solid solution series. *European Journal of Mineralogy* 2007; **19**: 65–73.

70. Romero MJ, Du H, Teeter G, Yan Y, Al-Jassim MM. Comparative study of the luminescence and intrinsic point defects in the kesterite Cu_2ZnSnS_4 and chalcopyrite $Cu(In,Ga)Se_2$ thin films used in photovoltaic applications. *Physical Review B—Condensed Matter and Materials Physics* 2011; **84**: 165324.

71. Scragg JJS, Choubrac L, Lafond A, Ericson T, Platzer-Björkman C. A low-temperature order–disorder transition in Cu_2ZnSnS_4 thin films. *Applied Physics Letters* 2014; **104**: 041911.

72. Rey G, Redinger A, Sendler J, Weiss TP, Thevenin M, Guennou M, El Adib B, Siebentritt S. The band gap of $Cu_2ZnSnSe_4$: effect of order–disorder. *Applied Physics Letters* 2014; **105**: 112106.

73. Gokmen T, Gunawan O, Todorov TK, Mitzi DB. Band tailing and efficiency limitation in kesterite solar cells. *Applied Physics Letters* 2013; **103**: 103506.

74. Halliday DP, Claridge R, Goodman MCJ, Mendis BG, Durose K, Major JD. Luminescence of Cu$_2$ZnSnS$_4$ polycrystals described by the fluctuating potential model. *Journal of Applied Physics* 2013; **113**: 223503.

75. Katahara JK, Hillhouse HW. Quasi-Fermi level splitting and sub-bandgap absorptivity from semiconductor photoluminescence. *Journal of Applied Physics* 2014; **116**: 173504.

76. Zawadzki P, Zakutayev A, Lany S. Entropy-driven clustering in tetrahedrally bonded multinary materials. *Physical Review Applied* 2015; **3**: 034007.

77. Teixeira JP, Sousa RA, Sousa MG, da Cunha AF, Fernandes PA, Salomé PMP, Leitão JP. Radiative transitions in highly doped and compensated chalcopyrites and kesterites: the case of Cu$_2$ZnSnS$_4$. *Physical Review B* 2014; **90**: .

78. Tanaka K, Shinji T, Uchiki H. Photoluminescence from Cu$_2$ZnSnS$_4$ thin films with different compositions fabricated by a sputtering-sulfurization method. *Solar Energy Materials and Solar Cells* 2014; **126**: 143–148.

79. Tanaka K, Miyamoto Y, Uchiki H, Nakazawa K, Araki H. Donor–acceptor pair recombination luminescence from Cu$_2$ZnSnS$_4$ bulk single crystals. *physica status solidi (a)* 2006; **203**: 2891–2896.

80. Hönes K, Zscherpel E, Scragg J, Siebentritt S. Shallow defects in Cu$_2$ZnSnS$_4$. *Physica B: Condensed Matter* 2009; **404**: 4949–4952.

81. Levcenko S, Tezlevan VE, Arushanov E, Schorr S, Unold T. Free-to-bound recombination in near stoichiometric Cu$_2$ZnSnS$_4$ single crystals. *Physical Review B* 2012; **86**: 045206.

82. Grossberg M, Krustok J, Raudoja J, Raadik T. The role of structural properties on deep defect states in Cu$_2$ZnSnS$_4$ studied by photoluminescence spectroscopy. *Applied Physics Letters* 2012; **101**: 102102.

83. Grossberg M, Salu P, Raudoja J, Krustok J. Microphotoluminescence study of Cu$_2$ZnSnS$_4$ polycrystals. *Journal of Photonics for Energy* 2013; **3**: 030599–030599.

84. Dirnstorfer I, Wagner M, Hofmann DM, Lampert MD, Karg F, Meyer BK. Characterization of CuIn(Ga)Se$_2$ thin films. *physica status solidi (a)* 1998; **168**: 163–175.

85. Yu PW. Excitation-dependent emission in Mg-, Be-, Cd-, and Zn-implanted GaAs. *Journal of Applied Physics* 1977; **48**: 5043–5051.

86. Levanyuk AP, Osipov VV. Edge luminescence of direct-gap semiconductors. *Soviet Physics Uspekhi* 1981; **24**: 187.

87. Leitão JP, Santos NM, Fernandes PA, Salomé PMP, da Cunha AF, González JC, Ribeiro GM, Matinaga FM. Photoluminescence and electrical study of fluctuating potentials in Cu$_2$ZnSnS$_4$-based thin films. *Physical Review B* 2011; **84**: 024120.

88. Vineyard GH. Theory of order–disorder kinetics. *Physical Review* 1956; **102**: 981–992.

89. Krämmer C, Huber C, Zimmermann C, Lang M, Schnabel T, Abzieher T, Ahlswede E, Kalt H, Hetterich M. Reversible order–disorder related band gap changes in Cu$_2$ZnSn(S,Se)$_4$ via post-annealing of solar cells measured by electroreflectance. *Applied Physics Letters* 2014; **105**: 262104.

90. Gürel T, Sevik C, Çağın T. Characterization of vibrational and mechanical properties of quaternary compounds Cu$_2$ZnSnS$_4$ and Cu$_2$ZnSnSe$_4$ in kesterite and stannite structures. *Physical Review B* 2011; **84**: 205201.

91. Mortazavi Amiri NB, Postnikov A. Electronic structure and lattice dynamics in kesterite-type Cu$_2$ZnSnSe$_4$ from first-principles calculations. *Physical Review B* 2010; **82**: 205204.

92. Khare A, Himmetoglu B, Cococcioni M, Aydil ES. First principles calculation of the electronic properties and lattice dynamics of Cu$_2$ZnSn(S$_{1-x}$Se$_x$)$_4$. *Journal of Applied Physics* 2012; **111**: 123704.

93. Khare A, Himmetoglu B, Johnson M, Norris DJ, Cococcioni M, Aydil ES. Calculation of the lattice dynamics and Raman spectra of copper zinc tin chalcogenides and comparison to experiments. *Journal of Applied Physics* 2012; **111**: 083707.

94. Valakh MY, Kolomys OF, Ponomaryov SS, Yukhymchuk VO, Babichuk IS, Izquierdo-Roca V, Saucedo E, Perez-Rodriguez A, Morante JR, Schorr S, Bodnar IV. Raman scattering and disorder effect in Cu$_2$ZnSnS$_4$. *physica status solidi (RRL)—Rapid Research Letters* 2013; **7**: 258–261.

95. Biswas K, Lany S, Zunger A. The electronic consequences of multivalent elements in inorganic solar absorbers: multivalency of Sn in Cu$_2$ZnSnS$_4$. *Applied Physics Letters* 2010; **96**: 201902.

96. Giraldo S, Neuschitzer M, Thersleff T, López-Marino S, Sánchez Y, Xie H, Colina M, Placidi M, Pistor P, Izquierdo-Roca V, Leifer K, Pérez-Rodríguez A, Saucedo E. Large efficiency improvement in Cu$_2$ZnSnSe$_4$ solar cells by introducing a superficial Ge nanolayer, *Advanced Energy Materials* 2015; 1501070. DOI:10.1002/aenm.201501070

97. Stølen S, Johnsen HB, Bøe CS, Karlsen OB, Grande T. Stable and metastable phase equilibria in the GeSe2–Se system. *Journal of Phase Equilibria* 1999; **20**: 17–28.

98. Kim I, Kim K, Oh Y, Woo K, Cao G, Jeong S, Moon J. Bandgap-graded Cu$_2$Zn(Sn$_{1-x}$Ge$_x$)S$_4$ thin-film

solar cells derived from metal chalcogenide complex ligand capped nanocrystals. *Chemistry of Materials* 2014; **26**: 3957–3965.

99. Ford GM, Guo Q, Agrawal R, Hillhouse HW. Earth abundant element $Cu_2Zn(Sn_{1-x}Ge_x)S_4$ nanocrystals for tunable band gap solar cells: 6.8% efficient device fabrication. *Chemistry of Materials* 2011; **23**: 2626–2629.

100. Guo Q, Ford GM, Yang W-C, Hages CJ, Hillhouse HW, Agrawal R. Enhancing the performance of CZTSSe solar cells with Ge alloying. *Solar Energy Materials and Solar Cells* 2012; **105**: 132–136.

101. Hages CJ, Levcenco S, Miskin CK, Alsmeier JH, Abou-Ras D, Wilks RG, Bär M, Unold T, Agrawal R. Improved performance of Ge-alloyed CZTGeSSe thin-film solar cells through control of elemental losses. *Progress in Photovoltaics: Research and Applications* 2015; **23**: 376–384.

102. Bag S, Gunawan O, Gokmen T, Zhu Y, Mitzi DB. Hydrazine-processed Ge-substituted CZTSe solar cells. *Chemistry of Materials* 2012; **24**: 4588–4593.

103. Li JB, Chawla V, Clemens BM. Investigating the role of grain boundaries in CZTS and CZTSSe thin film solar cells with scanning probe microscopy. *Advanced Materials* 2012; **24**: 720–3.

104. Kim GY, Jeong AR, Kim JR, Jo W, Son D-H, Kim D-H, Kang J-K. Surface potential on grain boundaries and intragrains of highly efficient $Cu_2ZnSn(S,Se)_4$ thin-films grown by two-step sputtering process. *Solar Energy Materials and Solar Cells* 2014; **127**: 129–135.

105. Yin W-J, Wu Y, Wei S-H, Noufi R, Al-Jassim MM, Yan Y. Engineering grain boundaries in $Cu_2ZnSnSe_4$ for better cell performance: a first-principle study. *Advanced Energy Materials* 2014; **4**: 1300712.

106. Gershon T, Shin B, Bojarczuk N, Hopstaken M, Mitzi DB, Guha S. The role of sodium as a surfactant and suppressor of non-radiative recombination at internal surfaces in Cu_2ZnSnS_4. *Advanced Energy Materials* 2015; **5**: 1400849.

107. Sutter-Fella CM, Stückelberger JA, Hagendorfer H, La Mattina F, Kranz L, Nishiwaki S, Uhl AR, Romanyuk YE, Tiwari AN. Sodium assisted sintering of chalcogenides and its application to solution processed $Cu_2ZnSn(S,Se)_4$ thin film solar cells. *Chemistry of Materials* 2014; **26**: 1420–1425.

108. Liu X, Cui H, Kong C, Hao X, Huang Y, Liu F, Song N, Conibeer G, Green M. Rapid thermal annealed Molybdenum back contact for Cu_2ZnSnS_4 thin film solar cells. *Applied Physics Letters* 2015; **106**: 131110.

109. Nagaoka A, Miyake H, Taniyama T, Kakimoto K, Nose Y, Scarpulla MA, Yoshino K. Effects of sodium on electrical properties in Cu_2ZnSnS_4 single crystal. *Applied Physics Letters* 2014; **104**: 152101.

110. Prabhakar T, Jampana N. Effect of sodium diffusion on the structural and electrical properties of Cu_2ZnSnS_4 thin films. *Solar Energy Materials and Solar Cells* 2011; **95**: 1001–1004.

111. Li JV, Kuciauskas D, Young MR, Repins IL. Effects of sodium incorporation in Co-evaporated $Cu_2ZnSnSe_4$ thin-film solar cells. *Applied Physics Letters* 2013; **102**: 163905.

112. Caballero R, Kaufmann CA, Eisenbarth T, Grimm A, Lauermann I, Unold T, Klenk R, Schock HW. Influence of Na on $Cu(In,Ga)Se_2$ solar cells grown on polyimide substrates at low temperature: impact on the $Cu(In,Ga)Se_2$/Mo interface. *Applied Physics Letters* 2010; **96**: 092104.

113. Salome PMP, Hultqvist A, Fjallstro V, Edoff M, Aitken B, Vaidyanathan K, Zhang K, Fuller K, Kosik WC. $Cu(In,Ga)Se_2$ solar cells with varying Na content prepared on nominally alkali-free glass substrates. *IEEE Journal of Photovoltaics* 2013; **3**: 852–858.

114. Schuler S, Siebentritt S, Nishiwaki S, Rega N, Beckmann J, Brehme S, Lux-Steiner MC. Self-compensation of intrinsic defects in the ternary semiconductor $CuGaSe_2$. *Physical Review B* 2004; **69**: 045210.

115. Tong Z, Yan C, Su Z, Zeng F, Yang J, Li Y, Jiang L, Lai Y, Liu F. Effects of potassium doping on solution processed kesterite Cu_2ZnSnS_4 thin film solar cells. *Applied Physics Letters* 2014; **105**: 223903.

116. Haight R, Shao X, Wang W, Mitzi DB. Electronic and elemental properties of the $Cu_2ZnSn(S,Se)_4$ surface and grain boundaries. *Applied Physics Letters* 2014; **104**: 033902.

117. Yoon J-H, Seong T-Y, Jeong J-h. Effect of a Mo back contact on Na diffusion in CIGS thin film solar cells. *Progress in Photovoltaics: Research and Applications* 2013; **21**: 58–63.

118. Zellner MB, Birkmire RW, Eser E, Shafarman WN, Chen JG. Determination of activation barriers for the diffusion of sodium through CIGS thin-film solar cells. *Progress in Photovoltaics: Research and Applications* 2003; **11**: 543–548.

119. Sardashti K, Haight R, Gokmen T, Wang W, Chang L-Y, Mitzi DB, Kummel AC. Impact of nanoscale elemental distribution in high-performance kesterite solar cells. *Advanced Energy Materials* 2015; **5**: 140218.

120. Barkhouse DAR, Haight R, Sakai N, Hiroi H, Sugimoto H, Mitzi DB. Cd-free buffer layer materials on $Cu_2ZnSn(S_xSe_{1-x})_4$: band alignments with ZnO, ZnS, and In_2S_3. *Applied Physics Letters* 2012; **100**: 193904–5.

121. Minemoto T, Matsui T, Takakura H, Hamakawa Y, Negami T, Hashimoto Y, Uenoyama T, Kitagawa M. Theoretical analysis of the effect of conduction band offset of window/CIS layers on performance of CIS solar cells using device simulation. *Solar Energy Materials and Solar Cells* 2001; **67**: 83–88.

122. Haight R, Barkhouse A, Gunawan O, Shin B, Copel M, Hopstaken M, Mitzi DB. Band alignment at the $Cu_2ZnSn(S_xSe_{1-x})_4$/CdS interface. *Applied Physics Letters* 2011; **98**: 253502.

123. Bär M, Schubert BA, Marsen B, Wilks RG, Pookpanratana S, Blum M, Krause S, Unold T, Yang W, Weinhardt L, Heske C, Schock HW. Cliff-like conduction band offset and KCN-induced recombination barrier enhancement at the CdS/Cu_2ZnSnS_4 thin-film solar cell heterojunction. *Applied Physics Letters* 2011; **99**: 222105.

124. Neuschitzer M, Sanchez Y, Olar T, Thersleff T, Lopez-Marino S, Oliva F, Espindola-Rodriguez M, Xie H, Placidi M, Izquierdo-Roca V, Lauermann I, Leifer K, Pérez-Rodriguez A, Saucedo E. Complex surface chemistry of kesterites: Cu/Zn reordering after Low temperature postdeposition annealing and its role in high performance devices. *Chemistry of Materials* 2015, DOI:10.1021/acs.chemmater.5b01473.

125. Hironiwa D, Matsuo N, Sakai N, Katou T, Sugimoto H, Chantana J, Tang Z, Minemoto T. Sputtered (Zn, Mg)O buffer layer for band offset control in $Cu_2ZnSn(S,Se)_4$ solar cells. *Japanese Journal of Applied Physics* 2014; **53**: 106502.

126. Törndahl T, Coronel E, Hultqvist A, Platzer-Björkman C, Leifer K, Edoff M. The effect of $Zn_{1-x}Mg_xO$ buffer layer deposition temperature on Cu(In,Ga)Se$_2$ solar cells: a study of the buffer/absorber interface. *Progress in Photovoltaics: Research and Applications* 2009; **17**: 115–125.

127. Törndahl T, Hultqvist A, Platzer-Björkman C, Edoff M. Growth and characterization of ZnO-based buffer layers for CIGS solar cells. *Proceedings of SPIE* 2010; **7603**: 76030D–1.

128. Kim J, Hiroi H, Todorov TK, Gunawan O, Kuwahara M, Gokmen T, Nair D, Hopstaken M, Shin B, Lee YS, Wang W, Sugimoto H, Mitzi DB. High efficiency Cu ZnSn(S,Se) solar cells by applying a double In$_2$S$_3$/CdS emitter. *Advanced Materials* 2014. DOI:10.1002/adma.201402373.

129. Gunawan O, Gokmen T, Mitzi DB. Suns-VOC characteristics of high performance kesterite solar cells. *Journal of Applied Physics* 2014; **116**: 084504.

130. Hiroi H, Sakai N, Kato T, Sugimoto H, High voltage Cu_2ZnSnS_4 submodules by hybrid buffer layer. in *IEEE 39th Photovoltaic Specialists Conference (PVSC)*. 2013.

131. Vora N, Blackburn J, Repins I, Beall C, To B, Pankow J, Teeter G, Young M, Noufi R. Phase identification and control of thin films deposited by co-evaporation of elemental Cu, Zn, Sn, and Se. *Journal of Vacuum Science & Technology, A: Vacuum, Surfaces, and Films* 2012; **30**: 051201.

132. Li W, Chen J, Yan C, Hao X. The effect of ZnS segregation on Zn-rich CZTS thin film solar cells. *Journal of Alloys and Compounds* 2015; **632**: 178–184.

133. Yin W-J, Wu Y, Noufi R, Al-Jassim M, Yan Y. Defect segregation at grain boundary and its impact on photovoltaic performance of CuInSe$_2$. *Applied Physics Letters* 2013; **102**: 193905.

134. Tanaka K, Oonuki M, Moritake N, Uchiki H. $Cu_2ZnSnS_4Cu_2ZnSnS_4$ thin film solar cells prepared by non-vacuum processing. *Solar Energy Materials and Solar Cells* 2009; **93**: 583–587.

135. Meysing DM, Wolden CA, Griffith MM, Mahabaduge H, Pankow J, Reese MO, Burst JM, Rance WL, Barnes TM. Properties of reactively sputtered oxygenated cadmium sulfide (CdS:O) and their impact on CdTe solar cell performance. *Journal of Vacuum Science & Technology, A: Vacuum, Surfaces, and Films* 2015; **33**: 021203.